Applied Physics Reviews

REVIEW ARTICLE | SEPTEMBER 16 2024

Advanced GeSe-based thermoelectric materials: Progress and future challenge

Special Collection: Frontiers in energy materials research: novel measurement, modelling and processing approaches

Tu Lyu ; Moran Wang; Xiaohuan Luo; Yuwei Zhou; Lei Chen ; Min Hong ; Lipeng Hu

Appl. Phys. Rev. 11, 031323 (2024)
https://doi.org/10.1063/5.0220462

View Online
Export Citation

Articles You May Be Interested In

Achieving glass-like lattice thermal conductivity in PbTe by $AgBiTe_2$ alloying

Appl. Phys. Lett. (December 2022)

Pressure-induced first order phase transition in bulk GeSe

J. Appl. Phys. (May 2020)

Designing high-efficiency metal and semimetal contacts to two-dimensional semiconductor γ-GeSe

Appl. Phys. Lett. (September 2022)

01 October 2024 06:40:17

Advanced GeSe-based thermoelectric materials: Progress and future challenge

Cite as: Appl. Phys. Rev. **11**, 031323 (2024); doi: 10.1063/5.0220462
Submitted: 25 May 2024 · Accepted: 21 August 2024 ·
Published Online: 16 September 2024

Tu Lyu,[1] Moran Wang,[1] Xiaohuan Luo,[1] Yuwei Zhou,[1] Lei Chen,[2] Min Hong,[2,a)] and Lipeng Hu[1,a)]

AFFILIATIONS

[1]College of Materials Science and Engineering, Guangdong Provincial Key Laboratory of Deep Earth Sciences and Geothermal Energy Exploitation and Utilization, Shenzhen University, Shenzhen 518060, People's Republic of China
[2]Center for Future Materials and School of Engineering, University of Southern Queensland, Springfield Central, Queensland 4300, Australia

Note: This paper is part of the APR Special Topic on Frontiers in energy materials research: novel measurement, modelling and processing approaches.
[a)]**Authors to whom correspondence should be addressed:** min.hong@unisq.edu.au and hulipeng@szu.edu.cn

ABSTRACT

GeSe, composed of ecofriendly and earth-abundant elements, presents a promising alternative to conventional toxic lead-chalcogenides and earth-scarce tellurides as mid-temperature thermoelectric applications. This review comprehensively examines recent advancements in GeSe-based thermoelectric materials, focusing on their crystal structure, chemical bond, phase transition, and the correlations between chemical bonding mechanism and crystal structure. Additionally, the band structure and phonon dispersion of these materials are also explored. These unique features of GeSe provide diverse avenues for tuning the transport properties of both electrons and phonons. To optimize electrical transport properties, the strategies of carrier concentration engineering, multi-valence band convergence, and band degeneracy established on the phase modulation are underscored. To reduce the lattice thermal conductivity, emphasis is placed on intrinsic weak chemical bonds and anharmonicity related to chemical bonding mechanisms. Furthermore, extra-phonon scattering mechanisms, such as the point defects, ferroelectric domains, boundaries, nano-precipitates, and the phonon mismatch originating from the composite engineering, are highlighted. Additionally, an analysis of mechanical properties is performed to assess the long-term service of thermoelectric devices based on GeSe-based compounds, and correspondingly, the theoretical energy-conversion efficiency is discussed based on the present zT values of GeSe. This review provides an in-depth insight into GeSe by retrospectively examining the development process and proposing future research directions, which could accelerate the exploitation of GeSe and elucidate the development of broader thermoelectric materials.

Published under an exclusive license by AIP Publishing. https://doi.org/10.1063/5.0220462

TABLE OF CONTENTS

I. INTRODUCTION 2
II. CRYSTAL STRUCTURE AND CHEMICAL BONDING MECHANISM 3
III. ELECTRONIC BAND STRUCTURE AND PHONON DISPERSION 5
A. Electronic band structure in different crystal structure 5
B. Phonon dispersion under different crystal structure 6
IV. THEORETICAL PREDICTION OF TE PERFORMANCE 8
V. STRATEGIES FOR OPTIMIZING ELECTRICAL TRANSPORT PERFORMANCE 9
A. Optimization of the carrier concentration 10
B. Electronic band structure manipulation 10
VI. REDUCTION OF LATTICE THERMAL CONDUCTIVITY 12
A. Intrinsically low thermal conductivity 13
1. Weak chemical bond 13
2. Strong lattice anharmonicity in MVB phase 13
B. Ferroelectric domains in rhombohedral GeSe 16
C. Phonon scattering via extra-scattering mechanisms 17
VII. COMPOSITE PHASE ENGINEERING 17
VIII. MECHANICAL PERFORMANCE AND ENERGY-CONVERSION EFFICIENCY 17
IX. SUMMARY AND OUTLOOK 17

01 October 2024 06:40:17

Published under an exclusive license by AIP Publishing

I. INTRODUCTION

The imminent global energy scarcity, coupled with the concurrent environmental challenges arising from extensive fossil energy consumption, catalyzes the exploration and advancement of sustainable green energy technologies.[1] A substantial portion of energy is wasted as heat by automotive engines and industrial emissions. This low-grade heat poses challenges for effective recycling and utilization, resulting in energy loss. Thermoelectric (TE) materials offer a viable solution for directly converting waste heat into usable electricity, or vice versa,[2–6] with the features of minimal greenhouse gas emissions, no moving components, noise-free operation, high reliability, suitability for miniaturization, and adaptability to extreme conditions, making them promising in power generation and solid-state refrigeration applications.[7–9] For example, radioisotope thermoelectric generators (RTGs) have demonstrated their practicality as power supply systems in both terrestrial applications and long-term space exploration projects.[10–12] Additionally, thermoelectric cooling modules play a crucial role in dissipating heat from micro-components, such as fifth-generation (5 G) optical communication chips.[13–15] This underscores the versatility and applicability of TE technology in diverse fields.

Motivated by their specific use as power source for spacecraft[16] and the potential applications in daily life, TE materials have garnered widespread attention and extensive research. Achieving the conversion between heat and electricity is by the thermoelectric devices, such as thermoelectric power generators (TEGs) and thermoelectric coolers (TECs). The maximum energy conversion efficiency (η_{max}) and the output power density (ω) for a TEG are expressed as

$$\eta_{max} = \frac{\Delta T}{T_H} \cdot \frac{\sqrt{1+Z\overline{T}}-1}{\sqrt{1+Z\overline{T}}+\frac{T_C}{T_H}}, \tag{1}$$

$$\omega = \frac{(T_H - T_C)^2}{4L}\alpha^2\sigma, \tag{2}$$

and the coefficient of performance (COP) for a TEC is expressed as

$$COP = \frac{T_C}{\Delta T} \cdot \frac{\sqrt{1+Z\overline{T}}-\frac{T_H}{T_C}}{\sqrt{1+Z\overline{T}}+1}, \tag{3}$$

where T_H and T_C are the hot- and cold-side temperatures, respectively. ΔT is the temperature difference between the hot and cold sides, defined by $\Delta T = T_H - T_C$. L is the length of the TE legs. $Z\overline{T}$ is the average value of the device ZT, defined as

$$Z\overline{T} = \frac{(\alpha_p - \alpha_n)^2\overline{T}}{\left(\sqrt{\kappa_p/\sigma_p} + \sqrt{\kappa_n/\sigma_n}\right)^2}. \tag{4}$$

Herein, α, σ, and κ are the Seebeck coefficient, electrical conductivity, and thermal conductivity of the TE materials, respectively. The subscripts of p and n represent p-type or n-type materials. For a single thermoelectric material, the dimensionless figure of merit (zT) is described as $zT = \alpha^2\sigma T/\kappa$,[17–21] where $\alpha^2\sigma$ is the power factor (PF), serving as the benchmark for electrical properties and influencing the device's output power,[22] κ is the sum of electronic thermal conductivity κ_e and lattice thermal conductivity κ_L, and T is the specific temperature in Kelvin. Achieving an excellent zT value, and consequently, high η_{max} and COP, requires a synergistic combination of high α and σ, alone with a low κ, all within a single material.[23–25] However, the strong interdependence among the parameters of α, σ and κ_e presents a formidable challenge in maximizing the zT value.

Significant efforts have been directed toward enhancing the TE performance of various environmentally friendly TE materials. Noteworthy examples include Bi_2Te_3 solid solutions,[26–30] chalcogenides,[31–37] $Mg_3(Sb,Bi)_2$ based materials,[38,39] half-Heusler alloys,[40–42] and SiGe alloys.[43,44] Electrically, recognizing the reciprocal relationship between σ and α with carrier concentration (n_H), appropriate doping levels are introduced to optimize n_H. This approach balances σ and α, thereby maximizing the PF.[45] Moreover, various strategies have proven to be effective in enhancing electrical properties. These include modulation doping and designing light band edges with low effective mass to enhance carrier mobility (μ_H),[46,47] as well as band engineering such as band convergence[48–50] and resonant state doping[51–53] to promote density-of-state effective mass. Turning attention to thermal considerations, significant interest has been directed toward reducing the independent parameter κ_L. In this context, inhibiting phonon transport by introducing multiscale phonon scattering centers has been widely embraced to minimize κ_L.[54–56] Examples include defect engineering involving zero-dimensional point defects (substitutions, vacancies, interstitials),[57–61] one-dimensional dislocations,[62,63] two-dimensional (2D) planar vacancies,[64] and three-dimensional (3D) nanoprecipitations.[65,66] Additionally, strategies such as nanostructuring, hierarchical architecturing, heavy element doping, weak chemical bonding, and the adoption of sophisticated crystal structures with high symmetry have been reported to reduce κ_L.[67] These diverse approaches collectively contribute to the advancement of TE materials across a spectrum of temperature applications.

Group IV–VI chalcogenides, exemplified by PbQ (Q = S, Se, Te),[68–73] GeTe,[74–77] SnTe,[61,78,79] and SnSe,[80–82] represent key constituents of high-performance TE materials designed for mid-temperature applications (500–800 K). In addition, GeSe, a compound within the Group IV–VI category, has emerged as a promising mid-temperature thermoelectric candidate, with theoretical predictions suggesting a potential zT of 2.5 at 800 K for an n_H of $\sim 10^{19}$ cm^{-3}.[83] However, GeSe has faced challenges in realizing its theoretical predicted zT values. This has led to limited attention for GeSe in thermoelectric applications, despite its extensive use in optoelectronics,[84] photovoltaic applications,[85] and resistive memory cells.[86]

Recent efforts have been dedicated to GeSe alloy to enhance its TE performance. To increase the n_H of p-type GeSe, aliovalent doping strategies have been employed as a core initiative.[87–89] In addition, GeSe undergoes phase transitions at elevated temperatures, high pressure, or via multi-component alloying. Specifically, the orthorhombic to the rhombohedral phase transition can be achieved at 1600 K or high pressure of 2 GPa.[90] This phase transition can be also achieved by alloying with I-V-VI_2 compounds.[91–94] In addition, a transformation from orthorhombic to cubic phase was achieved when temperature increased to 920–930 K[95] or at high pressure of 8 GPa.[90,96] Drawing inspiration from the successful crystal structure manipulation in GeTe[97] and SnSe,[98] comprehensive approaches involving crystal structure regulation, along with subsequent band and phonon engineering, have been implemented to improve the thermoelectric properties of GeSe. Figure 1 summarizes the current progress in developing GeSe-based TE materials, indicating a superior thermoelectric performance

01 October 2024 06:40:17

Published under an exclusive license by AIP Publishing

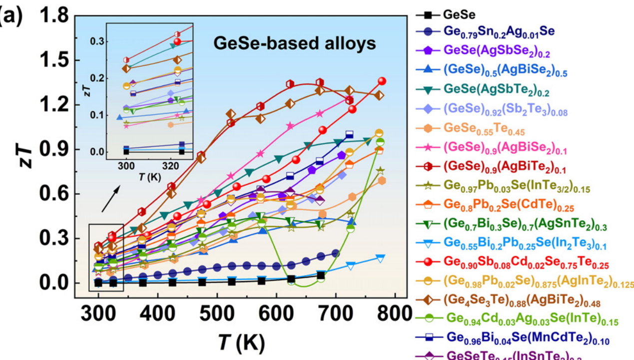

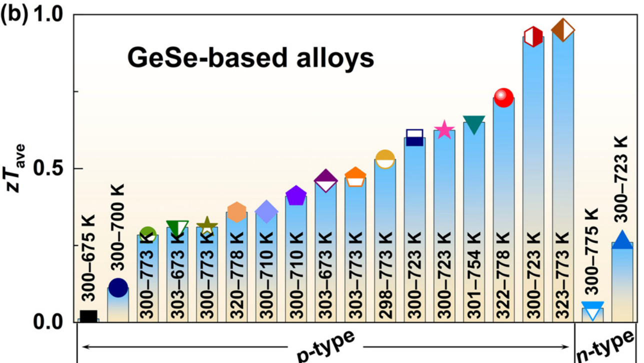

FIG. 1. Recent progress of GeSe-based TE materials. (a) Figure of merit (zT) as a function of temperature, (b) average zT of p-type pristine orthorhombic GeSe,[100] $Ge_{0.79}Sn_{0.2}Ag_{0.01}Se$,[87] rhombohedral $GeSe(AgSbSe_2)_{0.2}$,[91] $GeSe(AgSbTe_2)_{0.2}$,[92] $GeSe_{0.55}Te_{0.45}$,[101] $(GeSe)_{0.9}(AgBiSe_2)_{0.1}$,[94] $(GeSe)_{0.9}(AgBiTe_2)_{0.1}$,[93] $Ge_{0.97}Pb_{0.03}Se(InTe_{3/2})_{0.15}$,[102] $(Ge_{0.98}Pb_{0.02}Se)_{0.875}(AgInTe_2)_{0.125}$,[103] $Ge_{0.8}Pb_{0.2}Se(CdTe)_{0.25}$,[104] $Ge_{0.9}Sb_{0.08}Cd_{0.02}Se_{0.75}Te_{0.25}$,[99] $Ge_{0.96}Bi_{0.04}Se(MnCdTe_2)_{0.1}$,[105] $(Ge_4Se_3Te)_{0.88}(AgBiTe_2)_{0.48}$,[106] orthorhombic-rhombohedral dual-phases $Ge_{0.94}Cd_{0.03}Ag_{0.03}Se(InTe)_{0.15}$,[100] cubic $(GeSe)_{0.92}(Sb_2Te_3)_{0.08}$,[107] $GeSeTe_{0.15}(InSnTe_2)_{0.2}$,[108] $(Ge_{0.7}Bi_{0.3}Se)_{0.7}(AgSnTe_2)_{0.3}$,[109] and n-type $Ge_{0.55}Bi_{0.2}Pb_{0.25}Se(In_2Te_3)_{0.1}$,[110] $(GeSe)_{0.5}(AgBiSe_2)_{0.5}$.[111]

in the high-symmetry rhombohedral and cubic phases compared to the low-symmetry orthorhombic counterpart. To date, a state-of-the-art zT value of 1.36 at 778 K and a high average zT (zT_{ave}) of 0.73 between 322 and 778 K have been achieved in rhombohedral $Ge_{0.90}Sb_{0.08}Cd_{0.02}Se_{0.75}Te_{0.25}$.[99]

In this article, we review the recent advancements in GeSe-based TE materials and the cutting-edge strategies for performance enhancement. GeSe-based TE materials exhibit significant promise in achieving high performance and establishing efficient TE devices for widespread applications, owing to the utilization of environmentally friendly and abundantly available elements. The elucidated strategies presented herein aim to guide research endeavors in the pursuit of high-performance thermoelectric candidates across diverse material categories. The initial section of this review encapsulates a summary of GeSe's characterizations, encompassing the crystal structure and phase transitions, chemical bonding mechanism, as well as electronic band structure, and phonon dispersion property. Following the theoretical prediction of TE performance and experimental strategies for performance enhancement are discussed, i.e., carrier concentration manipulation, and band engineering. Afterward, we investigate the methods for reducing κ_L, covering the intrinsically advantageous soft chemical bond and lattice anharmonicity that are related to chemical bonding mechanisms, and phonon scattering by point defects, domains, precipitations, and phonon mismatch from phase boundary. This review also extends to an examination of the mechanical properties of GeSe-based compounds, providing insights into their long-term durability as TE device assemblies. Ultimately, we draw conclusions and propose future research directions for GeSe.

II. CRYSTAL STRUCTURE AND CHEMICAL BONDING MECHANISM

GeSe embraces three crystal structures of orthorhombic, rhombohedral, and cubic phases, as depicted in Figs. 2(a)–2(c). The orthorhombic phase is stable under ambient conditions and has lattice parameters of $a = 4.38$ Å, $b = 3.82$ Å, and $c = 10.79$ Å, with the space group of *Pnma*.[112] By increasing temperature or physical pressure, GeSe transforms to either rhombohedral phase with the space group of *R3m* or cubic phase with the space group of *Fm-3m*.[90,95,96] In orthorhombic GeSe, the crystal structure reveals alternating metal and nonmetal atoms occupying lattice sites, forming a chair-like polygon configuration with threefold Ge/Se units sharing vertices.[113] It also shows the puckered sheets along the a axis direction, interconnected by weak van der Waals interactions.[96] In the cubic phase, the Ge atom is coordinated with six neighboring Se atoms, while in the rhombohedral counterpart, the Ge atom is bonded with three closer and three farther Se atoms.

Another difference among these structures can be found from the perspective of the primitive cell, as depicted in Figs. 2(d)–2(f). The orthorhombic GeSe includes one vertical and two horizontal Ge–Se bonds, showcasing equivalent bond lengths of 2.59 Å with the bond angles of 93°. The coordination number of orthorhombic is three, smaller than that of rhombohedral and cubic GeSe with the coordination number of six. Additionally, the transformation from cubic to rhombohedral GeSe induces a displacement of the central Ge atom from (0.5, 0.5, 0.5) to (0.5-δ, 0.5-δ, 0.5-δ), concomitant with a reduction in the axis angle from 60° to 58°, resembling the configuration of cubic GeTe.[7]

The phase transition fundamentally hinges on chemical bonding mechanisms.[114–116] To understand the fundamental nature of chemical bonding, a comprehensive 2D map originated from a quantum-mechanical principle has been devised to show the electron sharing (ES) and electron transferring (ET),[117,118] as depicted in Fig. 3(a). This map visually distinguishes between covalent, metallic, and ionic bonding. Covalently bonded materials exhibit dominant electron-sharing behavior, resulting in stable electron configurations through the sharing of electron pairs and often involving s–p orbital hybridization.[119] Conversely, in ionic compounds, chemical bonding is primarily governed by ET, leading to the formation of positively and negatively charged ions. Metallic systems exhibit complete electron delocalization, minimizing charge localization through both ES and ET.[117] Additionally, metavalent bonding (MVB) occupies a distinct region on the map, showcasing characteristics distinct from traditional bonding types. MVB involves the sharing of approximately one electron between neighboring atoms, accompanied by moderate electron transfer, demonstrating both characteristics of localization and delocalization.[120,121] MVB is defined by the establishment of a half-filled σ-bond between p-orbital electrons, and the s-band exhibits lower energy

01 October 2024 06:40:17

Published under an exclusive license by AIP Publishing

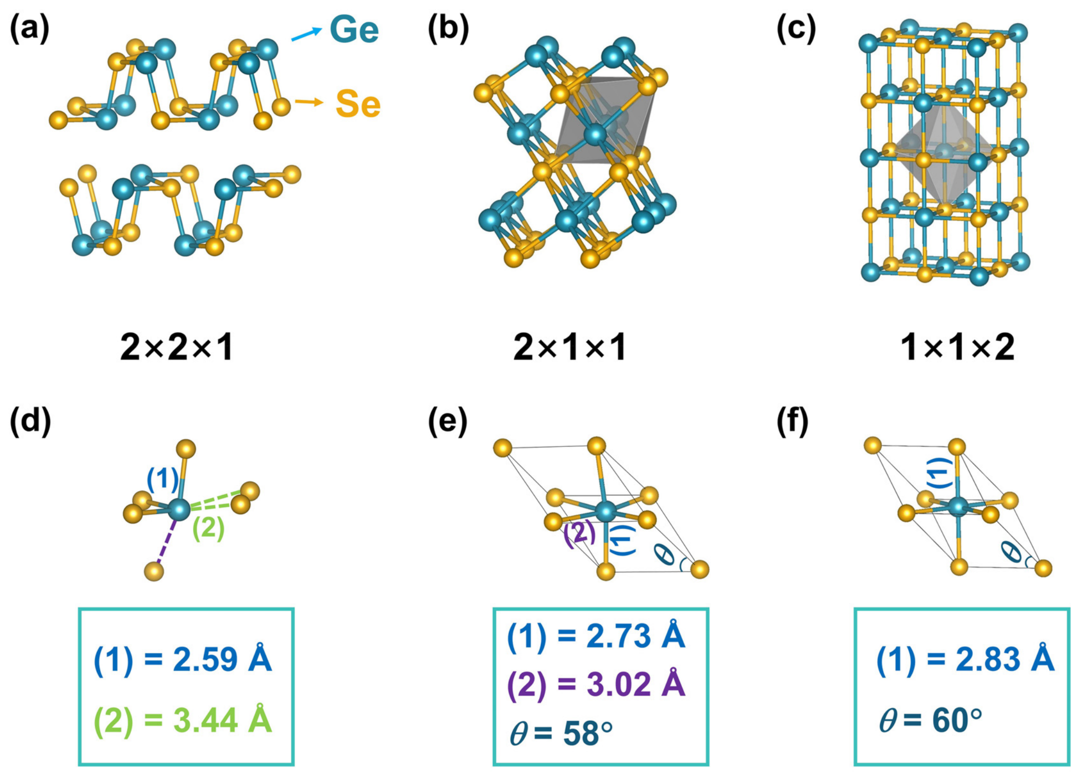

FIG. 2. Crystal structures of GeSe. The supercells are built based on conventional cells of (a) orthorhombic, (b) rhombohedral, and (c) cubic GeSe. Primitive cells of (d) orthorhombic, (e) rhombohedral, and (f) cubic GeSe.

01 October 2024 06:40:17

compared to the *p*-band. This unique configuration imparts structural characteristics to MVB compounds mainly manifested in an octahedrally arranged cubic or rhombohedral phase.

In GeSe, the orthorhombic phase utilizes covalent bonding, whereas the rhombohedral and cubic counterparts prominently feature the unique MVB.[100] This alteration in the chemical bonding mechanism is attributed to the varying degree of *p*-orbital electrons bonding and a simultaneous reduction in the lattice distortion, a parameter often quantified as Peierls distortion (PD).[123] Specifically, PD is expressed as the ratio of long to short bonds, denoted as $PD = r_l/r_s$, as illustrated in Fig. 3(b). For instance, the inhibition of PD leads to a gradual shift from covalent bonding to MVB, accompanied by a concurrent phase transition from orthorhombic to rhombohedral or even cubic.[121,124]

A previous study has further indicated the chemical bonding mechanisms of orthorhombic, rhombohedral, and cubic GeSe by calculating their ES and ET values, revealing crucial insights illustrated in Fig. 3(a).[122] In this context, the orthorhombic GeSe resides near the connecting line, exhibiting a large ES value (lack of ET) indicative of covalent bonding ($PD = 1.36$) with a discernible ionic contribution. Conversely, cubic GeSe manifests an ideal octahedral configuration, situated on the dashed green line with the lowest ES value, signifying a pure MVB nature ($PD = 1$). Furthermore, the green region between the red region and green dashed line, representing GeSe compounds with a distorted octahedral arrangement, features a smaller ES value and a moderate $PD = 1.13$. This region typically corresponds to a rhombohedral crystal structure. Generally, electrons of rock salt cubic structure exhibit delocalization but can be localized by the Peierls distortion effect.[123] This means that the metavalently bonded rhombohedral or cubic phase has more delocalization than the covalently bonded orthorhombic one. This provides the opportunity to identify the chemical bonding and, thereby, the crystal structure via an electron localization function (ELF) analysis, which has been used to analyze orthorhombic GeSe and rhombohedral GeSe alloys with $AgInTe_2$ and Pb, as depicted in Figs. 3(c) and 3(d).

Additionally, the chemical bonding mechanisms of GeSe can be experimentally discerned through atom probe tomography (APT) technology by evaluating the probability of multiple events (PME).[125–127] The PME quantifies the probability of displacing multiple ions by breaking chemical bonds during a laser pulse.[125,128,129] A large PME value (generally greater than 60%) serves as a distinctive indicator of MVB in chalcogenides.[127,129,130] Conversely, PME values below 30% are associated with alternative bonding mechanisms such as covalent or ionic bonding. Figure 3(e) illustrates the APT characterization of binary GeSe and the $GeAg_xSb_xSe_{1+2x}$ systems with $x = 0.10$ and 0.15.[122] Notably, binary orthorhombic GeSe demonstrates a comparatively lower PME value, whereas the $x = 0.15$ sample exhibits a higher PME value, signifying the presence of the metavalently bonded rhombohedral phase. In contrast, the $x = 0.10$ sample displays distinct regions with varying PME values, corresponding to its orthorhombic and rhombohedral phases identified by X-ray diffraction (XRD). Similarly, a high PME value is also shown in rhombohedral

Published under an exclusive license by AIP Publishing

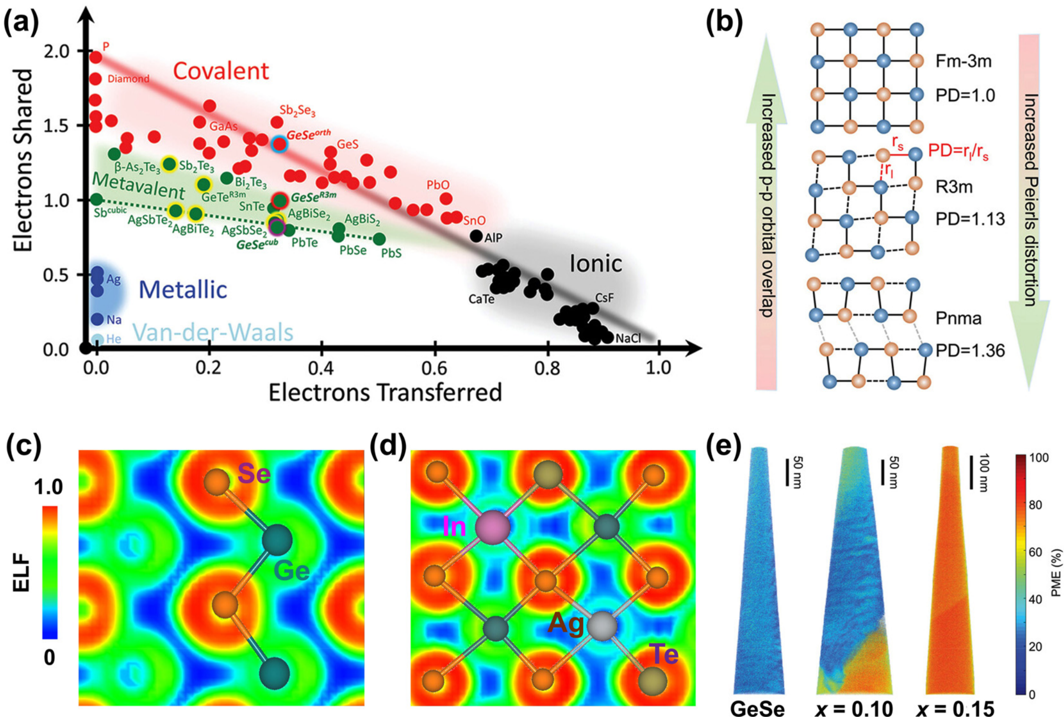

FIG. 3. (a) A two-dimensional (2D) map of the electron sharing (ES) and electron transferring (ET) for several solid-state materials. The distinct chemical bonding mechanism is differentiated by colors. (b) Schematic diagram of the variation of Peierls distortion (PD) for cubic GeSe, rhombohedral GeSe, and orthorhombic GeSe. Electron localization functions (ELFs) of (c) orthorhombic GeSe and (d) rhombohedral $Ge_{20}PbAg_3In_3Se_{21}Te_6$. (e) Three-dimensional (3D) probability of multiple events (PME) plot for $GeAg_xSb_xSe_{1+2x}$ samples ($x = 0$, 0.10, and 0.15) by atom probe tomography (APT) measurement, which indicates the variation of chemical bonding mechanisms in different GeSe phases. Panels (a), (b), and (e) reproduced with permission from Yu *et al.*, Adv. Mater. **35**(19), 2300893 (2023). Copyright 2023 Wiley-VCH.[122] Panels (c) and (d) reproduced with permission from Huang *et al.*, Interdiscip. Mater. **3**(4), 607–620 (2024). Copyright 2024 Wiley-VCH.[103]

$Ge_{0.8}Pb_{0.2}Se(CdTe)_{0.25}$, indicating the presence of MVB in the rhombohedral phase.[104]

III. ELECTRONIC BAND STRUCTURE AND PHONON DISPERSION

A. Electronic band structure in different crystal structure

In addition to elucidating the crystal structure of GeSe, understanding its band structure is paramount for comprehending its thermoelectric properties. Figures 4(a)–4(c) present the calculated band structures of orthorhombic, rhombohedral, and cubic GeSe, which encompasses a detailed breakdown of orbital contribution, including Ge-*s*, Ge-*p*, Ge-*d*, Se-*s*, Se-*p*, and Se-*d* orbitals.[122] Notably, orthorhombic GeSe manifests as an indirect semiconductor with the valence band maximum (VBM) located along the Γ-Z direction while the conduction band minimum (CBM) suited at Γ point. By contrast, the rhombohedral and cubic GeSe phases are direct semiconductors, as their VBM and CBM concurrently align at the L point. In addition, the orbital-resolved patterns highlight the predominant presence of *p*-orbital electrons from both Ge and Se in the conduction and valence bands approaching the Fermi level across all crystal structures. The existence of Ge *s*-state at the valence band edge in orthorhombic GeSe suggests the *s*–*p* hybridization. By contrast, the rhombohedral and cubic GeSe indicate a weaker *s*–*p* hybridization than that in the orthorhombic phase. The weak *s*–*p* hybridization coupled with delocalized *p*-state electrons constitutes crucial features of MVB, which exerts a pronounced impact on thermoelectric performance.

The MVB materials are often referred to as incipient metals, exhibiting a half-filled σ-bond between *p*-orbital electrons, which results in metallic transport behavior with intrinsically no bandgap (E_g).[131] In contrast, the strong Peierls distortion in orthorhombic GeSe reduces *p*–*p* orbital overlap, favoring an enlarged E_g.[117] Therefore, the orthorhombic GeSe embraces a larger E_g than that in rhombohedral and cubic phases, as shown in Figs. 4(a)–4(c). This result is also corroborated by optical measurements, revealing a larger E_g of 1.1 eV for orthorhombic GeSe[132,133] compared to 0.40 eV for rhombohedral $(GeSe)_{0.9}(AgBiTe_2)_{0.1}$.[93] The large E_g of orthorhombic GeSe is unfavorable for electrical performance. Specifically, employing $k\cdot p$ perturbation theory to obtain the band dispersive curve and band effective mass (m_b*) near the band edge underscores the significance of a small E_g for a lower m_b*. This is intuitively discerned by the description of the Kane band model,

$$\frac{\hbar k^2}{2m^*} = E\left(1 + \frac{E}{E_g}\right), \tag{5}$$

where E, k, and $\hbar$ represent the energy, the wave vector, and the reduced Planck's constant, respectively.[134,135] The large E_g accompanied by the increased m_b^* has been indicated in lead chalcogenides.[136]

01 October 2024 06:40:17

Published under an exclusive license by AIP Publishing

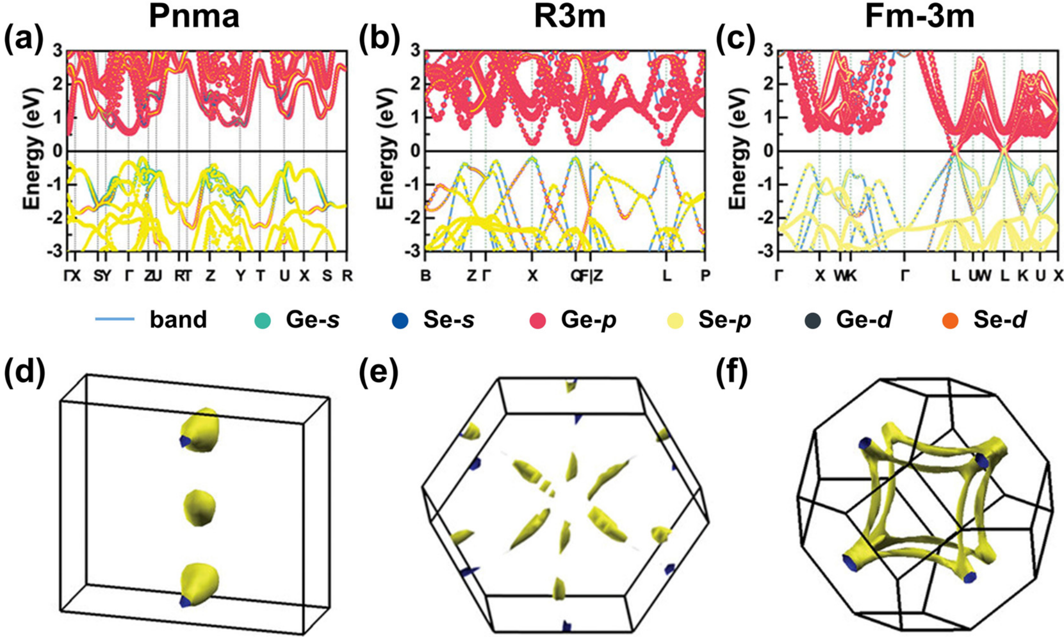

FIG. 4. Electronic band structures of GeSe. (a)–(c) Orbital-resolved band structures of orthorhombic, rhombohedral, and cubic GeSe. (b)–(d) Corresponding Fermi surfaces for these GeSe phases. Reproduced with permission from Yu *et al.*, Adv. Mater. **35**(19), 2300893 (2023). Copyright 2023 Wiley-VCH.[122]

Therefore, the anticipated lower m_b^* and, thus, the increased μ_H in rhombohedral and cubic GeSe, due to the shrinkage of E_g, favorably support the high electrical conductivity.

The diverse crystal structures observed in GeSe reflect varying degrees of Peierls distortion and exhibit different levels of symmetry and consequently the first Brillouin zone. Figures 4(d)–4(f) visually present Fermi surface images within the first Brillouin zone for orthorhombic, rhombohedral, and cubic GeSe, highlighting the dissimilar band degeneracy (N_v) arising from the valence band (VB) contributions. The N_v serves as the important parameter that signifies the capacity to achieve optimal electrical performance. Specifically, large N_v correlates with a high density-of-state effective mass (m_d^*) by the equation $m_d^* = N_v^{2/3} m_b^*$,[137] subsequently enhancing the α according to the Mott relationship. In the orthorhombic GeSe, the first valence band maximum (defined as VB_1) along the Γ-Z direction exhibits a N_v of 2, while the second valence band maximum (VB_2) embraces a N_v of 1. This means that the N_v of orthorhombic GeSe can achieve 3 after introducing the high doping level. However, the low solid solubility in orthorhombic GeSe attributed to its feature of strong ion–covalent bonding, occasions more challenges for a dramatic enhancement in n_H. Consequently, the orthorhombic GeSe only attains an effective N_v of 2.[103]

In comparison, the rhombohedral and cubic GeSe enhance the crystal symmetry, accordingly, modifying the first Brillouin zone and achieving a larger N_v compared to orthorhombic GeSe. Specifically, the cubic GeSe embraces eight half-symmetric pockets at the L point. Additionally, by introducing the doping level to promote the multiple band convergence, the Σ band with a total of 12 pockets can also be involved in conduction, yielding a large N_v of 16 in cubic GeSe.[107] However, considering that the rhombohedral GeSe derives from the distorted cubic phase along the [111] direction, the resultant symmetry breaking induces the split of the original L band and Σ band in cubic GeSe, similar to that observed in GeTe.[138] Consequently, the rhombohedral GeSe acquires a smaller N_v compared to the cubic GeSe. As observed in Fig. 4(e), the Fermi surface image of rhombohedral GeSe shows a total N_v of 9, arising from the six half pockets at the L point and six full pockets along the degenerate Σ band.[139] Consequently, from the perspective of the electronic band structure, engineering metavalently bonded rhombohedral and cubic GeSe by mitigating the Peierls distortion, and promoting the participation of multiple valence bands in carrier transport, further proves a significant advantage in enhancing electrical properties.

B. Phonon dispersion under different crystal structure

Figure 5 illustrates the computed phonon dispersions of GeSe. As depicted in Fig. 5(a), the dynamic stability of orthorhombic GeSe is evident, marked by the absence of imaginary vibrational modes. The phonon spectrum of orthorhombic GeSe reveals two sets of phonon modes with equal counts, spanning from 0 to 3.7 THz and 4.5 to 7.2 THz.[96] A notable feature is the presence of a "phonon bandgap" that distinctly separates the phonon modes at lower and upper frequencies, a phenomenon observed in various germanium-chalcogenides.[140] A study reported that in the orthorhombic GeSe, the acoustic modes along Γ-X direction characterizes *a* axis, while the directions along Γ-Y and Γ-Z represent the *b* and *c* axis, respectively.[83] The analysis of sound velocity that corresponds to the slope of acoustic phonon dispersions indicates a lower sound velocity along the *a* axis than that along the *b* and *c* axes in orthorhombic GeSe. This discrepancy suggests a softer mode along the *a* axis, signifying weaker interatomic bonding and pronounced anharmonicity: a characteristic feature

01 October 2024 06:40:17

Published under an exclusive license by AIP Publishing

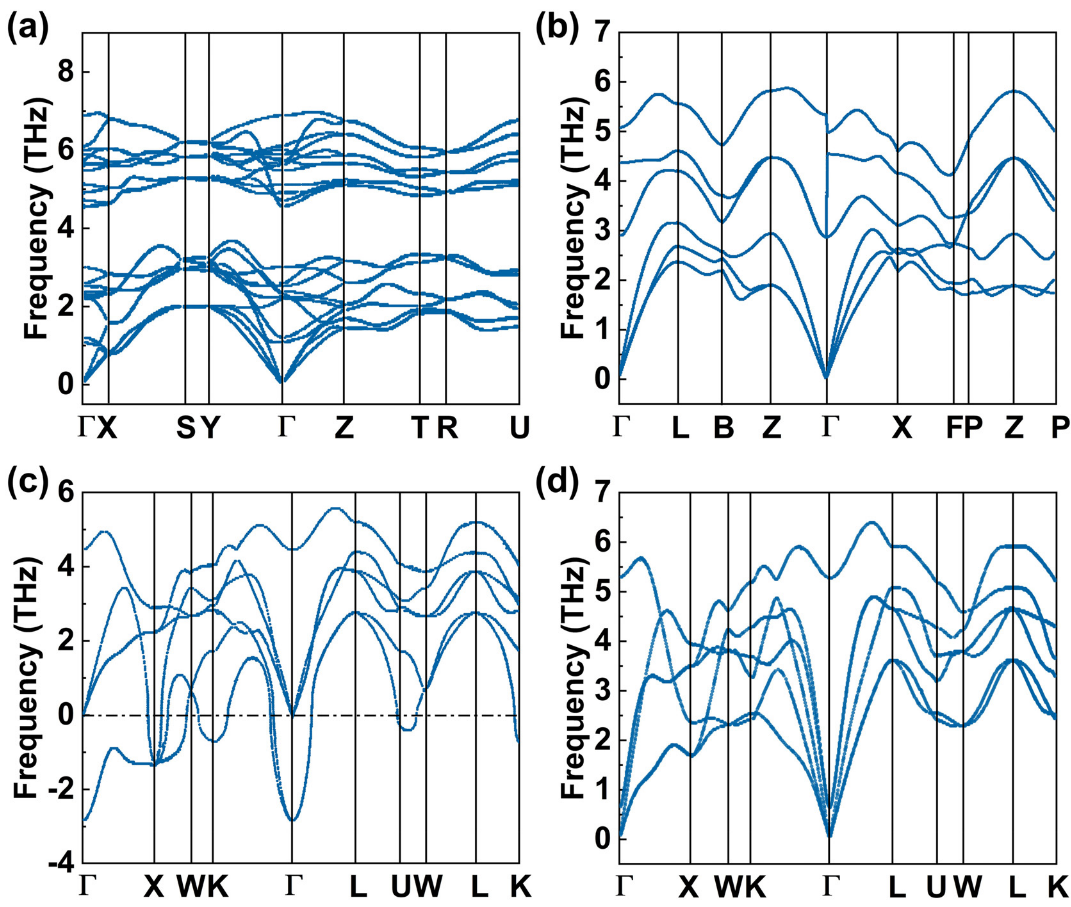

FIG. 5. Phonon dispersions of different GeSe phases. Phonon dispersion curves of (a) orthorhombic GeSe and (b) rhombohedral GeSe. Phonon dispersions of cubic GeSe (c) at ambient conditions and (d) under the pressure of 8 GPa. Panel (a) reproduced with permission from Deringer *et al.*, Phys. Rev. B **89**(9), 094303 (2014). Copyright 2014 American Physical Society.[96] Panel (b) reproduced with permission from Argaman *et al.*, CrystEngComm **19**(41), 6107–6115 (2017). Copyright 2017 The Royal Society of Chemistry.[141] Panels (c) and (d) reproduced with permission from Yu *et al.*, NPG Asia Mater. **10**(9), 882–887 (2018). Copyright 2018 Nature Publishing Group.[90]

attributed to the existence of van der Waals gaps along this direction. Consequently, the inherent anharmonicity may result in a relatively low κ_L in orthorhombic GeSe.[83]

Similarly, in the case of rhombohedral GeSe, all phonon modes exhibit positive frequencies along the high symmetrical direction of the Brillouin zone, indicative of dynamic stabilization in the *R3m* phase [Fig. 5(b)].[141] The dispersions at the lowest frequencies at the Γ point encompass two transverse acoustic branches (in-plane TA and out-of-plane ZA) and one longitudinal acoustic branch (LA), while the optical modes are situated in the higher-frequency region. A noteworthy departure from pristine rhombohedral GeTe, which features an acoustic-optical frequency gap leading to reduced phonon-phonon scattering,[75] the phonon spectrum of rhombohedral GeSe demonstrates a gapless transition between acoustic and optical branches, promoting inherent phonon scattering and thereby reducing κ_L. Additionally, the phonon dispersions curves of rhombohedral GeSe reveal a splitting of the longitudinal optical mode (LO) and transverse optical mode (TO), attributed to the incorporation of dipole–dipole interactions into the dynamic matrix.[139] Moving on to the calculated phonon dispersion relations of cubic GeSe as illustrated in Fig. 5(c), a significant number of phonon modes manifest as imaginary eigenvalues concentrated at the high symmetry Γ point within the Brillouin zone. This observation suggests inherent instability in cubic GeSe under ambient conditions,[96] making it experimentally unattainable. However, the dynamic instabilities of the cubic phase can be effectively suppressed by applying physical pressure. Figure 5(d) illustrates the disappearance of imaginary modes under an external pressure of 8 GPa, while real frequency components remain largely unchanged between ordinary and high pressure. This aligns with the concept that the orthorhombic phase in ambient conditions can transform into the cubic phase under high pressure.[90] A distinct feature in cubic GeSe as compared to rhombohedral counterpart is the crossing of optical modes into the acoustic modes. This phenomenon is conducive to strengthening optical phonons–acoustic phonons interactions, further contributing to the reduction of κ_L. Understanding these phonon characteristics provides valuable insights into the material's thermal transport properties and offers potential avenues for tuning and optimizing its κ_L.

01 October 2024 06:40:17

Published under an exclusive license by AIP Publishing

IV. THEORETICAL PREDICTION OF TE PERFORMANCE

The extremely low n_H in orthorhombic GeSe arising from the inherently high formation energy of Ge vacancy (E_v) and a large bandgap (E_g), coupled with inadequate μ_H, collectively contribute to the inferior TE performance, reaching a mere zT of 0.05 at 673 K.[105] Theoretical calculations have been utilized to predict the figure of merit zT of GeSe, considering varying n_H, to evaluate the prospective improvement in its TE performance. The density functional theory (DFT) calculations demonstrate that heavy hole doping induces a shift of the Fermi level toward the valence band, which facilitates active participation of the second valence band and creates additional carrier pockets for enhancing electrical transport, as shown in Fig. 6(a). The contribution from multiple bands leads to a slower decrease in the α with the increasing n_H, while σ experiences a significant increase at higher n_H levels. This results in a peak zT value of 0.8 at room temperature and 2.5 at 800 K along b axis in orthorhombic GeSe when n_H increases to 6.5×10^{19} cm^{-3},[83] comparable to the high TE performance of SnSe,[80,98] as depicted in Fig. 6(b).

The TE performance of p-type and n-type GeSe has also been comprehensively predicted by DFT calculations and Boltzmann transport theory. This predictive analysis involves an evaluation of electrical transport properties by calculating the charge density distributions near the Fermi level and the relaxation time. As depicted in Fig. 6(c), the iso-surface distribution of band-decomposed charge density at the VBM and CBM, with a charge density of 0.003 eÅ^{-3}, illustrates the establishment of a charge density channel for the CBM within n-type GeSe, which is conducive to electron transport.[142] This indicates the favorable σ along the a axis direction for n-type GeSe. By contrast, in the case of p-type GeSe, there is a lack of carrier transport routes in the interlayer, which impedes the hole transport and gives rise to a relatively low σ along this direction. Furthermore, the comparatively large relaxation time observed for n-type GeSe as illustrated in Fig. 6(d), further demonstrates the more favorable carrier transport within this variant. In addition, the relaxation time as a function of temperature signifies the stronger scattering at elevated temperatures, contributing to a decreasing trend in σ with increasing temperature, which corresponds to the experimental result. Consequently, in combination with the calculated electrical and thermal performance, the zT value of p-type GeSe stands at 0.6 under the n_H of 1×10^{20} cm^{-3} at 700 K, while for n-type GeSe, it reaches 2.5 with an n_H of 4×10^{19}cm^{-3} at 700 K, as shown in Fig. 6(e).[142]

The highly symmetric rhombohedral and cubic forms of GeSe exhibit larger band degeneracy compared to their orthorhombic counterpart, leading to a larger m_d^* and consequently the higher α.[103,107] A prediction for p-type and n-type rhombohedral GeSe is investigated by Tang *et al.*[139] Figure 7 shows the calculated σ, α, PF and zT values of p-type and n-type rhombohedral GeSe at different n_H and temperatures (300 and 800 K). Figure 7(a) suggests that the σ of p-type GeSe is

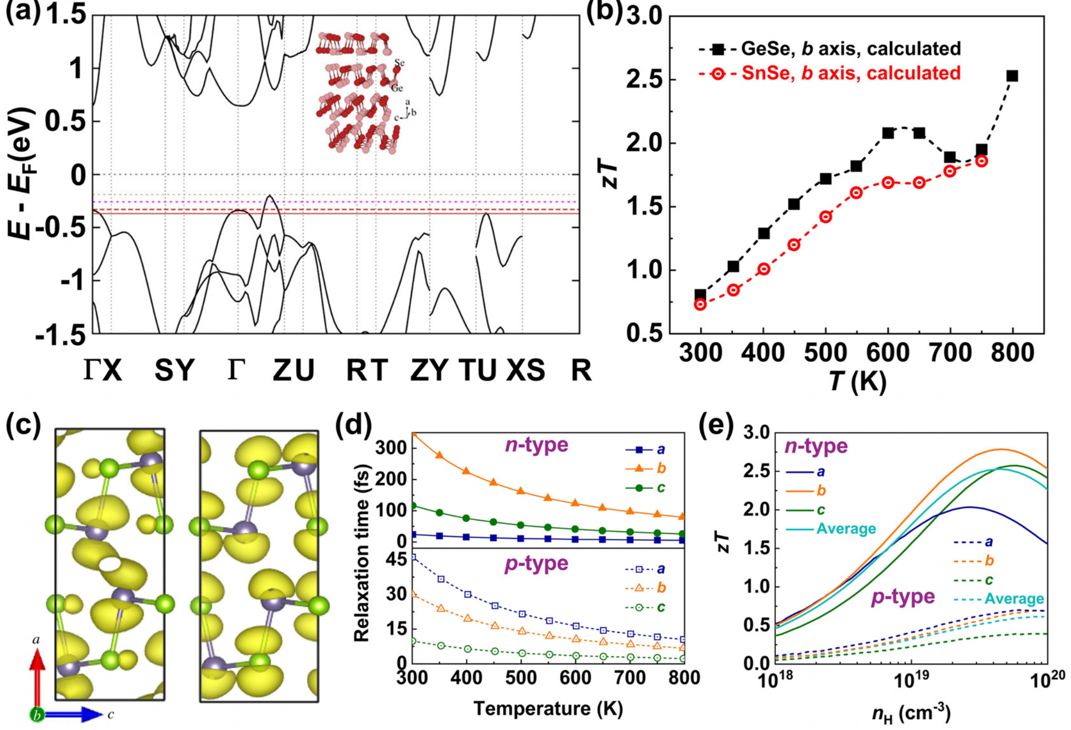

FIG. 6. (a) Electronic band structure of orthorhombic GeSe, showing the Fermi level shifts into the second valence band, as well as the variation of the Fermi surface after heavy hole doping. (b) Predicted temperature-dependent zT value of GeSe and SnSe. (c) Charge densities of GeSe with the left panel showing CBM and the right panel showing VBM. (d) Relaxation time as a function of temperature and (e) theoretical zT value as a function of n_H for n-type and p-type GeSe. Panels (a) and (b) reproduced with permission from Hao *et al.*, Chem. Mater. **28**(9), 3218–3226 (2016). Copyright 2016 American Chemical Society.[83] Panels (c)–(e) reproduced with permission from Fan *et al.*, R. Soc. Open Sci. **8**(6), 201980 (2021). Copyright 2021 The Royal Society Publishing.[142]

01 October 2024 06:40:17

Published under an exclusive license by AIP Publishing

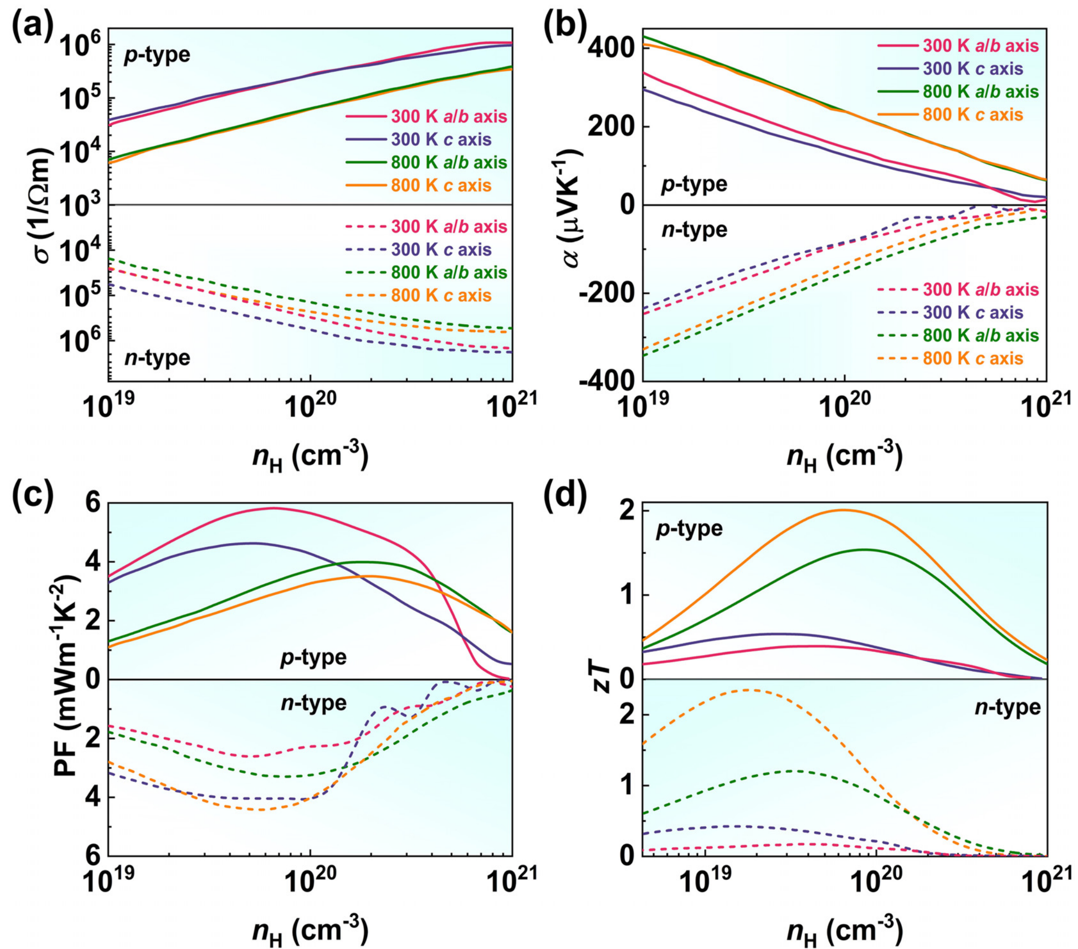

FIG. 7. Calculated thermoelectric properties of rhombohedral GeSe. (a) Electrical conductivity (σ), (b) Seebeck coefficient (α), (c) power factor (PF), and (d) figure of merit (zT) as a function of carrier concentration (n_H) for p-type and n-type counterparts along different axes at 300 and 800 K. Reproduced with permission from Yuan *et al.*, Phys. Chem. Chem. Phys. **22**(4), 1911–1922 (2020). Copyright 2020 Royal Society of Chemistry.[139]

smaller compared to its n-type counterpart at the same n_H. Additionally, σ of p-type GeSe is roughly identical alone both the a/b and c axes, whereas n-type GeSe exhibits a significant anisotropy in σ, with a larger value along the c axis than the a/b axis. Figure 7(b) depicts the α as a function of n_H, showcasing a larger value in p-type GeSe than in n-type one at the same temperature and n_H. The interplay between the increased σ and decreased α leads to a peak PF at the appropriate n_H, as depicted in Fig. 7(c). The maximum PF of p-type GeSe is 5.86 mW m^{-1} K^{-2} at 300 K and 4.05 mW m^{-1} K^{-2} at 800 K along the a/b axis, achieved under the n_H of 7.23×10^{19} cm^{-3} and 2.11×10^{20} cm^{-3}, respectively. By contrast, the optimal PF of n-type GeSe is observed along the c axis, reaching 4.09 mW m^{-1} K^{-2} at 300 K and 4.45 mW m^{-1} K^{-2} at 800 K with the n_H of 9.27×10^{19} cm^{-3} and 5.86×10^{19} cm^{-3}, respectively. Combining with the calculated κ, the predicted maximum zT value of p-type and n-type GeSe is 2.02 and 2.37 at 800 K [Fig. 7(d)]. The excellent TE performance of GeSe makes it a promising material for thermoelectric applications.

V. STRATEGIES FOR OPTIMIZING ELECTRICAL TRANSPORT PERFORMANCE

The electrical properties of GeSe can be enhanced by traditional carrier concentration engineering and electronic band engineering such as the multiple valence-bands convergence, similar to other Group IV–VI compounds.[143–146] Given the sophisticated crystal structures and their unique features in GeSe, various methodologies for enhancing electrical performance are established based on the manipulation of these crystal structures. Furthermore, the higher symmetry of crystal structures is associated with increased valley degeneracy (N_v)[147] and multiple valence bands[148,149] compared to their lower symmetry counterparts, which provides an additional avenue for advancing electrical properties. In this study, we probe into n_H optimization through aliovalent doping and the regulation of native Ge vacancies. Subsequently, we explore the impact of manipulating band structures on electrical transport performance, considering the interplay between crystal structures and chemical doping.

Published under an exclusive license by AIP Publishing
01 October 2024 06:40:17

A. Optimization of the carrier concentration

The principal reason for the inferior zT of orthorhombic GeSe stems from a large E_g and an ultralow n_H, which leads to a low PF.[87,105] Therefore, increasing n_H is pivotal in enhancing zT of GeSe. One promising approach for improving n_H in p-type GeSe is aliovalent doping on the Ge site. In this context, Cu, Ag, and Na are selected as potential acceptor dopants.[87–89] However, these elements fail to optimize n_H to the desired level ($\sim 10^{19}\,cm^{-3}$) due to the low solid solubility in orthorhombic GeSe, and the obtained zT has not been notably increased.[87]

Regulation of native cation vacancies can optimize n_H in p-type materials through appropriate chemical doping to tune the formation energy of cation vacancies (E_v), as observed with the doping of Pb in pristine GeTe and SnTe.[152–154] However, E_v of orthorhombic GeSe cannot be amended due to the low solid solubility of dopants. Alternatively, E_v is closely related to crystal symmetry. Figure 8(a) summarizes the dependence of n_H on crystal symmetry in many Group IV–VI compounds, indicating a high n_H in the high symmetric materials. DFT calculations reveal a gradual decrease in E_v with increasing crystal symmetry in GeSe. Specifically, E_v values of orthorhombic, rhombohedral, and cubic GeSe are 4.43, 3.72, and 3.57 eV, as depicted in Fig. 8(b). Therefore, a large n_H is likely to occur in high symmetric phases.[105] Additionally, the reduction in E_v increases the Ge vacancy concentration, which in turn favors a lower energy state of the system [Fig. 8(c)], thereby promoting the stability of the high crystal symmetry phase.[105] This phenomenon has also been found in cubic GeSe. Figure 8(d) shows the calculated formation enthalpy (ΔH), illustrating that the absolute value of ΔH ($|\Delta H|$) is largest for the orthorhombic phase in pure GeSe, while $|\Delta H|$ is largest for the cubic phase in the sample with the existence of Ge vacancy.[107]

To establish the correlation of n_H, crystal structure, and electrical properties, we summarize n_H of GeSe across three crystal structures in the context of various alloying compounds (such as Ag-IV-VI_2). The results are displayed in Fig. 8(e), revealing that highly symmetric rhombohedral and cubic phases exhibit larger n_H. For example, the n_H of $\sim 10^{16}\,cm^{-3}$ is achieved in orthorhombic GeSe, which increases to $\sim 10^{20}\,cm^{-3}$ for rhombohedral and cubic GeSe. Due to the increased n_H, the PF of rhombohedral and cubic GeSe is much higher than that in the orthorhombic counterpart, as illustrated in Fig. 8(f). In comparison with the theoretical curves calculated by the single parabolic band (SPB) model,[155] $Ge_{1-y}Bi_ySe(MnCdTe_2)_x$ and $GeSeTe_y(InSnTe_2)_x$ samples demonstrate an optimized n_H of $\sim 10^{20}\,cm^{-3}$ and enhanced PF. Consequently, the highest PF at room temperature of 583 and 512 $\mu W\,m^{-1}\,K^{-2}$ is achieved in rhombohedral $Ge_{0.96}Bi_{0.04}Se(MnCdTe_2)_{0.1}$[105] and cubic $GeSeTe_{0.15}(InSnTe_2)_{0.2}$.[108]

Reducing the T_c of phase transformation from orthorhombic to rhombohedral or cubic structures toward room temperature could significantly increase n_H by several orders of magnitude and consequently the PF. Given the intrinsic relation between crystal structure and chemical bonding mechanism, the suppression of T_c in GeSe can be achieved through the regulation of chemical bonding via doping or alloying. As exemplified by $GeSe_{1-x}Te_x$, increasing Te content can promote the transformation from orthorhombic phase to hexagonal phase and then to rhombohedral phase based on the phase diagram of the Ge-Se-Te system as shown in Fig. 9(a).[101,156] This phase transition may arise from the reduced energy difference of p-orbital electrons between Ge and Te compared to that between Ge and Se. Thus, the introduction of Te benefits the formation of MVB with strong p–p orbital interaction.

Notably, alloying $AgBiTe_2$ in GeSe has been shown to stabilize rhombohedral and cubic phases at room temperature, as depicted in Fig. 9(b), where X-ray diffraction patterns illustrate the transformation from orthorhombic to rhombohedral and cubic structures.[93] Similarly, the XRD analysis and the Rietveld refinement of c/a value also indicated a gradual orthorhombic-rhombohedral phase transition with the increasing $AgInTe_2$ content and additional Pb doping, as displayed in Figs. 9(c) and 9(d).[103] In addition, the stable and pure cubic phases have also been achieved through the alloying of Sb_2Te_3 and $InSnTe_2$ in p-type GeSe.[107,108] The reduction in T_c significantly enhances TE performance, as summarized in Table I, showcasing the experimental TE parameters for GeSe alloys with different crystal structures. Specifically, GeSe alloying with Ag-V-VI_2 (V = Bi, Sb; VI = Te, Se) compounds promotes the formation and stabilization of the rhombohedral phase at room temperatures, achieving a significantly enhanced zT value of 0.86–1.35.[91–94] In addition, employing multi-component alloying also improved the zT value to around or over 1, such as $MnCdTe_2$-Bi co-doping,[105] CdTe-Pb co-doping,[104] $AgInTe_2$-Pb co-doping,[103] $LiBiTe_2$ alloying,[157] and so on. At present, the state-of-the-art zT value was achieved in rhombohedral $Ge_{0.9}Sb_{0.08}Cd_{0.02}Se_{0.75}Te_{0.25}$, reaching 1.36 at 778 K.[99] The remarkable increase in zT values in the high-symmetry rhombohedral phase encourages continued exploration of the TE performance of GeSe and other materials undergoing phase transitions.

B. Electronic band structure manipulation

The electronic band structure has a significant influence on TE performance. As illustrated in Fig. 10(a), an overview of the characteristics of Group IV–VI binary compounds shows that E_g of cubic and rhombohedral lead-chalcogenides and tellurides is much smaller than the orthorhombic (Ge, Sn)(Se, S) systems,[63,83,158–163] in which the former indicates an excellent electrical properties and consequently the high zT. Therefore, an appropriate E_g is conducive to promoting the enhancement of electrical transport performance. For GeSe, the intricate crystal structures provide opportunities for regulating E_g and, thus, the TE performance through phase transitions. Specifically, strong Peierls distortion and electron transfer contribute to the opening E_g,[116,117] resulting in a large DFT calculated E_g of $\sim$0.81 eV for orthorhombic GeSe, higher than the rhombohedral counterpart with an optimal E_g of $\sim$0.39 eV and a much lower E_g in the cubic phase.[105] The E_g in rhombohedral GeSe approaches the high TE performance of rhombohedral GeTe, which contains the suitable E_g of 0.47 eV corresponding to the 6–10 k_BT_o rule, where k_B is the Boltzmann constant and T_o is the operation temperature.

Similar to the exceptional thermoelectric materials GeTe, multiple valence band edges can be responsible for the TE performance of GeSe, as schematically depicted in Fig. 10(b). However, the existence of a significant ΔE between VB_1 and VB_2 weakens the contribution of the VB_2 to electrical transport.[75] Therefore, manipulating the band structure to reduce the ΔE between multiple bands, aka the band convergence, has successfully indicated the efficacy for enhancing electrical properties. Generally, chemical doping is feasible to perform band structure engineering. However, the low solid solubility of orthorhombic GeSe confines the effect of dopants on band structures. In contrast, rhombohedral GeSe provides more space for chemical doping,[100] which demonstrates the opportunity of manipulating the band

01 October 2024 06:40:17

Published under an exclusive license by AIP Publishing

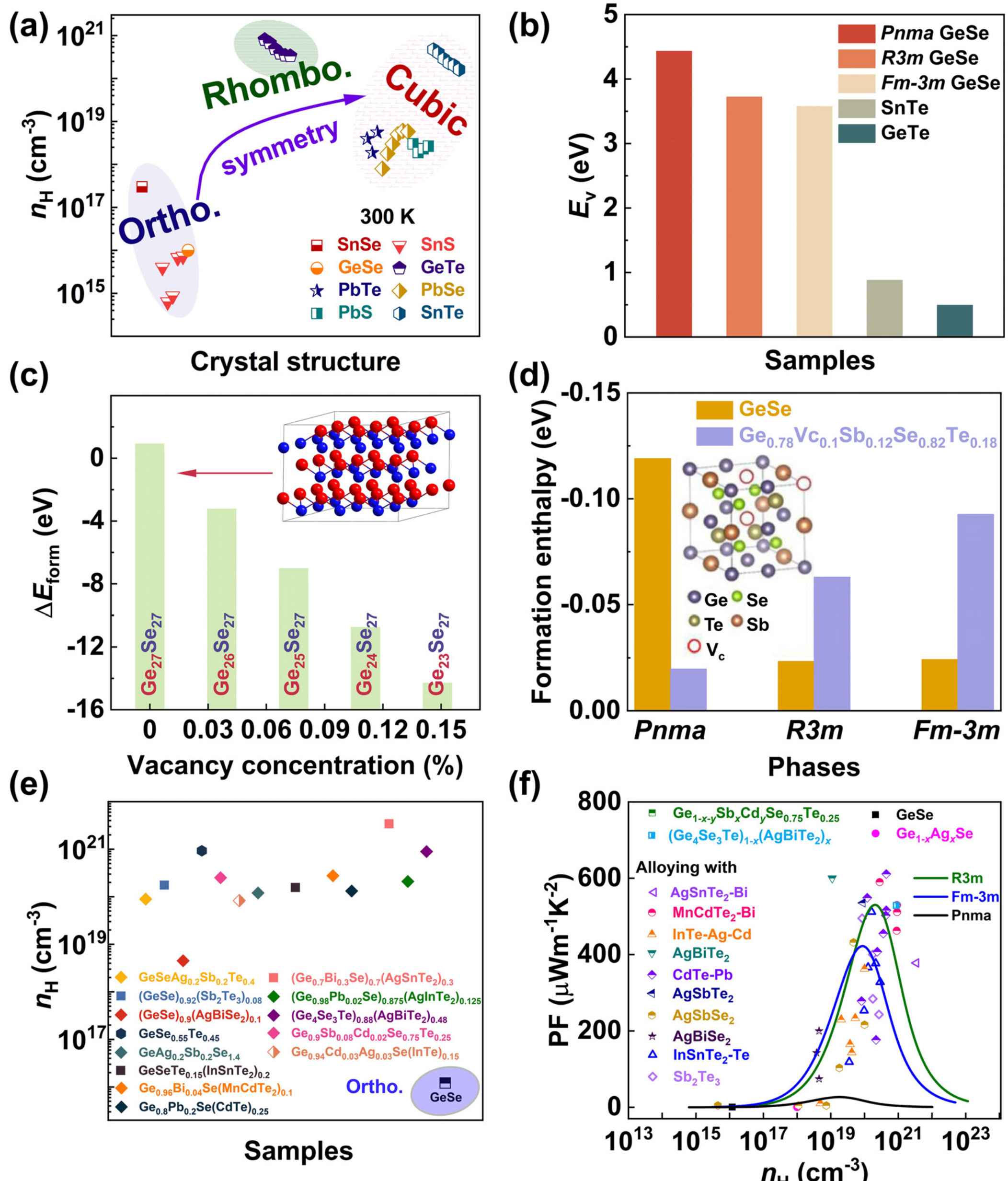

FIG. 8. (a) Carrier concentration (n_H) of representative binary group IV–VI compounds with different crystal structures. (b) The formation energy of cation vacancy (E_V) of orthorhombic, rhombohedral, and cubic GeSe,[105] as well as their comparison with SnTe[150] and GeTe.[151] (c) Formation energy of rhombohedral GeSe by removing different numbers of Ge atoms. (d) Calculated formation enthalpy of orthorhombic, rhombohedral, and cubic phases of GeSe and $Ge_{0.78}Vc_{0.1}Sb_{0.12}Se_{0.82}Te_{0.18}$, Vc represents the vacancy. (e) Carrier concentration (n_H) of GeSe-based TE materials in different crystal structures.[91,92,94,99–101,103–109] The square indicates the cubic phase, the diamond signifies the rhombohedral phase, and half-right diamonds represent orthorhombic-rhombohedral dual phases. (f) Calculated power factor (PF) vs carrier concentration (n_H) curves of orthorhombic, rhombohedral, and cubic GeSe using a single parabolic band (SPB) model.[87,91–94,99,100,104–109] The plots are the experimental results. Panels (a) and (c) reproduced with permission from Li *et al.*, Nano Energy **100**, 107434 (2022). Copyright 2022 Elsevier.[105] Panel (d) reproduced with permission from Yan *et al.*, J. Energy Chem. **45**, 83–90 (2020). Copyright 2020 Elsevier.[107]

structure via phase transition. Prior experimental evidence indicates that alloying CdTe effectively promotes the phase transition from orthorhombic to rhombohedral in GeSe. Calculated band structures of CdTe and Pb co-alloyed GeSe exhibit a reduced ΔE of 0.10 eV between VB_1 and VB_2,[104] lower than that in binary rhombohedral GeSe with a ΔE of 0.24 eV, as observed in Fig. 10(c). This reduced ΔE is also lower than that found in rhombohedral GeTe (0.15 eV)[164] and cubic PbTe (0.15 eV).[165] $AgInTe_2$ can also induce the phase transition and the

01 October 2024 06:40:17

Published under an exclusive license by AIP Publishing

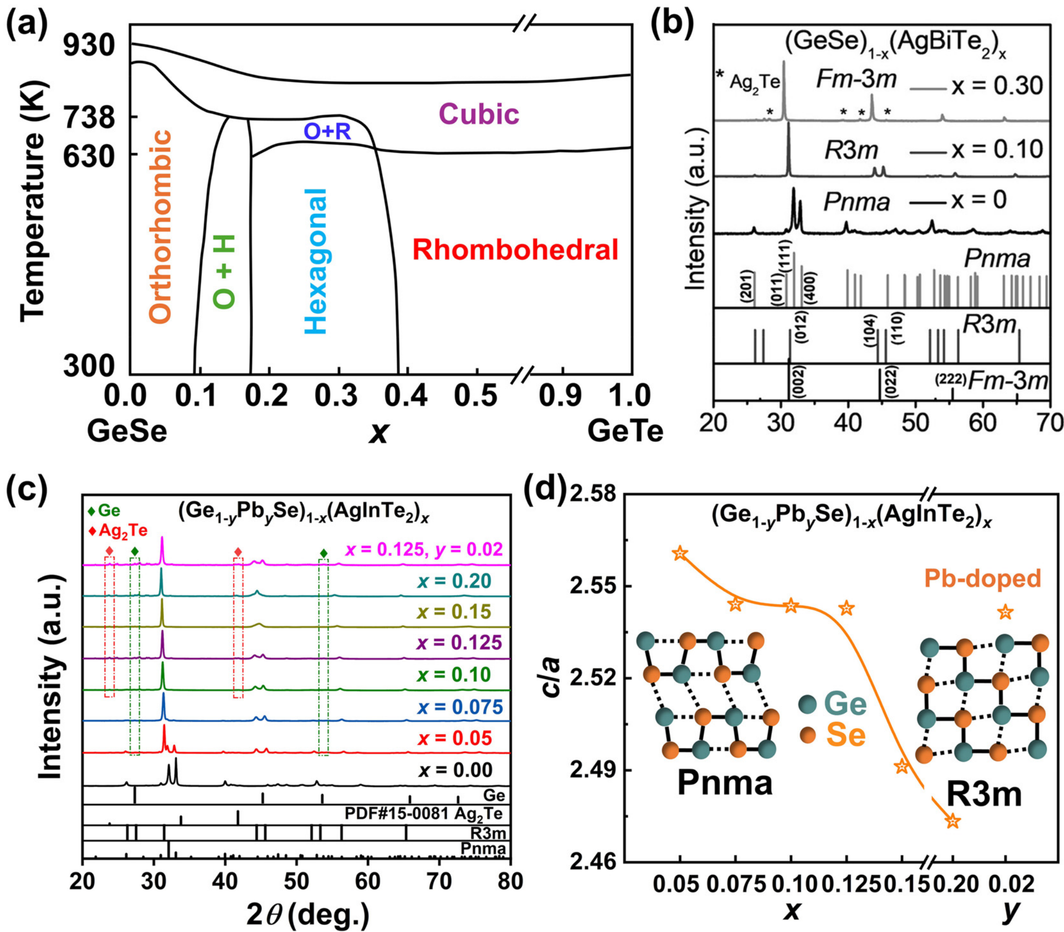

FIG. 9. (a) Phase diagram of the Ge-Se-Te system. (b) XRD patterns of $(GeSe)_{1-x}(AgBiTe_2)_x$ ($x = 0$, 0.10, and 0.30). (c) XRD patterns of $(Ge_{1-y}Pb_ySe)_{1-x}(AgBiTe_2)_x$ and (d) the Rietveld refinement of *c*/*a* value. Panel (a) reproduced with permission from Wang *et al.*, ACS Appl. Mater. Interfaces **12**(37), 41381–41389 (2020). Copyright 2020 American Chemical Society.[101] Panel (b) reproduced with permission from Sarkar *et al.*, Angew. Chem., Int. Ed. **60**(38), 10350–10358 (2021). Copyright 2021 Wiley-VCH.[93] Panels (c) and (d) reproduced with permission from Huang *et al.*, Interdiscip. Mater. 3(4), 607–620 (2024). Copyright 2024 Wiley-VCH.[103]

multiple band convergence in GeSe. GeSe alloying with $AgInTe_2$ promotes the formation of a rhombohedral phase, which remarkably modifies the band structure.[103] As depicted in Fig. 10(d), $Ge_{21}Ag_3In_3Se_{21}Te_6$ presents a reduced ΔE approximately to 0 eV, and the three valence bands of L, Σ, and Z bands simultaneously engage in electrical transport, leading to an optimized electrical performance. Additionally, the band convergence is also achieved by alloying GeSe with $AgSbTe_2$,[92] $AgBiTe_2$,[93] and $AgBiSe_2$,[94] as well as in Ge_4Se_3Te alloys with $AgBiTe_2$.[106]

The convergence of multiple bands aims to enhance the N_v.[166–168] As mentioned in Fig. 4(d), the small N_v of 2 is achieved in orthorhombic GeSe. In contrast, the convergence of L and Σ bands results in a larger N_v of 9 in rhombohedral GeSe.[103] This elevated N_v is favorable for achieving a large m_d^*. The calculated room-temperature Pisarenko curves of GeSe-based materials using the SPB model are illustrated to represent the variation of m_d^* with the phase structure and alloying compounds. As shown in Fig. 10(e), an upward movement in the $\alpha \sim n_H$ curves after alloying indicates an enhanced m_d^*, increasing from $0.71m_e$ for orthorhombic GeSe to 1.30–$5.54m_e$ for rhombohedral and cubic counterparts.[91,92,99,100,102–108] The remarkable increase in m_d^* reflects the band convergence, thereby strengthening the contribution to PF from the second valence band. Figure 10(f) displays PF as a function of the temperature of typical samples. As we can see, the room temperature PF can reach 490 $\mu W\ m^{-1}\ K^{-2}$ in $(Ge_{0.98}Pb_{0.02}Se)_{0.875}(AgInTe_2)_{0.125}$ sample when the ΔE is decreased to $\sim$0 eV.

VI. REDUCTION OF LATTICE THERMAL CONDUCTIVITY

In addition to enhancing electrical properties, reducing κ_L can also increase zT.[169,170] The κ_L can be described as $\kappa_L = 1/3\ C_p v^2 \tau$ with three parameters of specific heat C_p, sound velocity v, and relaxation time τ of phonons.[171] Among these parameters, C_p is generally defined as a constant when the temperature is significantly higher than the Debye temperature, which is estimated via the Dulong–Petit limit.[172] Therefore, the reduction of κ_L is generally achieved by inhibiting τ via strong phonon scattering and decreasing v via lattice softening or

01 October 2024 06:40:17

Published under an exclusive license by AIP Publishing

TABLE I. Maximum zT values and corresponding thermoelectric parameters for the present GeSe-based alloys.

Samples	Type	Phase	T (K)	zT_{max}	α ($\mu V K^{-1}$)	σ ($S m^{-1}$)	κ ($W m^{-1} K^{-1}$)	κ_L ($W m^{-1} K^{-1}$)
GeSe[100]	p	*Pnma*	673	0.05	673	103	0.61	0.61
$Ge_{0.79}Sn_{0.2}Ag_{0.01}Se$[87]	p	*Pnma*	700	0.2	460	537	0.4	0.39
$Ge_{0.94}Na_{0.01}Ag_{0.05}Se$[89]	p	*Pnma*	630	⋯	646	5.58	0.26	0.26
$(GeSe)_{0.9}(AgBiSe_2)_{0.1}$[94]	p	*R3m*	723	1.25	223	28 333	0.81	0.48
$GeAg_{0.2}Sb_{0.2}Se_{1.4}$[91]	p	*R3m*	710	0.86	263	15 860	0.91	0.73
$(GeSe)_{0.9}(AgBiTe_2)_{0.1}$[93]	p	*R3m*	627	1.35	243	21 373	0.59	0.38
$GeSeAg_{0.2}Sb_{0.2}Te_{0.4}$[92]	p	*R3m*	754	0.96	231	24 169	1.01	0.71
$Ge_{0.96}Bi_{0.04}Se(MnCdTe_2)_{0.1}$[105]	p	*R3m*	723	≈ 1	217	25 571	0.91	0.60
$Ge_{0.8}Pb_{0.2}Se(CdTe)_{0.25}$[104]	p	*R3m*	773	0.9	225	17 529	0.77	0.55
$Ge_{0.9}Sb_{0.08}Cd_{0.02}Se_{0.75}Te_{0.25}$[99]	p	*R3m*	778	1.36	262	29 500	1.16	0.78
$Ge_{0.97}Pb_{0.03}Se(InTe_{3/2})_{0.15}$[102]	p	*R3m*	773	0.76	233	15 539	0.86	0.66
$(Ge_{0.98}Pb_{0.02}Se)_{0.875}(AgInTe_2)_{0.125}$[103]	p	*R3m*	773	1.0	189	31 387	0.86	0.45
$(Ge_4Se_3Te)_{0.88}(AgBiTe_2)_{0.48}$[106]	p	*R3m*	723	1.30	198	38 300	0.83	0.41
$Ge_{0.94}Cd_{0.03}Ag_{0.03}Se(InTe)_{0.15}$[100]	p	*Pnma-R3m*	773	0.95	236	16 600	0.79	0.58
$(Ge_{0.7}Bi_{0.3}Se)_{0.7}(AgSnTe_2)_{0.3}$[109]	p	*Fm-3m*	573	0.46	149	33 500	0.94	0.60
$GeSeTe_{0.15}(InSnTe_2)_{0.2}$[108]	p	*Fm-3m*	573	0.62	190	23 511	0.79	0.56
$(GeSe)_{0.92}(Sb_2Te_3)_{0.08}$[107]	p	*Fm-3m*	710	0.73	193	35 081	1.27	0.83
$Ge_{0.55}Bi_{0.2}Pb_{0.25}Se(In_2Te_3)_{0.1}$[110]	n	*Fm-3m*	773	0.18	−93	18 710	0.73	0.45
$(GeSe)_{0.5}(AgBiSe_2)_{0.5}$[111]	n	*Fm-3m*	677	0.45	−183	11 885	0.61	0.43

introduction of a large mass of atoms. Additionally, intrinsic attributes of materials, such as lattice anharmonicity, also empower the phonon–phonon scattering, thereby suppressing κ_L. Herein, we highlight the representative strategies of intrinsic weak chemical bond and lattice anharmonicity, as well as the lattice defects scattering and the extrinsic impurity scattering, delving into their respective impacts on reducing κ_L in GeSe.

A. Intrinsically low thermal conductivity

1. Weak chemical bond

The chemical bonding mechanism and, thus, the crystal symmetry have a significant effect on intrinsic κ_L by consideration of bond strength. The bond strength is associated with the bulk modulus, the Debye temperature, and the bond length.[173] The three crystal structures of GeSe employ different chemical bonding mechanisms, specifically, the orthorhombic GeSe exhibits covalent bonding, while the rhombohedral and cubic counterparts adopt MVB.[122] In contrast to the covalent bonding utilizing the electron pairs between adjacent atoms,[119] the metavalently bonded compounds are characterized by p–p orbital electrons bonding with weak s–p hybridization, forming a half-filled σ-bond between the adjacent atoms.[100] This causes the rhombohedral and cubic GeSe to exhibit an octahedral configuration, with a longer bond than that in tetrahedrally bonded materials, indicative of weaker chemical bonding. Moreover, these materials generally have lower bulk modulus and Debye temperatures as compared to the covalently bonded compounds, highlighting the preference for weaker chemical bonding in MVB compounds,[173] for instance, in rhombohedral $Ge_{1-y}Pb_ySe(CdTe)_x$ systems.[104]

2. Strong lattice anharmonicity in MVB phase

The low κ_L in high-symmetry GeSe with a light atomic mass of Ge and Se is mainly attributed to its MVB nature, which exhibits the softening of optical mode and strong lattice anharmonicity.[173] A significant characterization for metavalently bonded materials is the highly delocalized electron density distribution, which results in large Born effective charge, electronic polarization, and optical dielectric constant.[173] The large Born effective charge in metavalently bonded rhombohedral GeSe,[122] conveying a signal of separation between LO phonons and TO phonons.[68,174] Furthermore, the MVB phase with highly delocalized p-orbital electrons promotes the dramatic coupling between electrons and TO phonons, thereby resulting in the softening of TO modes.[173] This leads to a strong lattice anharmonicity and, thereby, the significant phonon scattering,[175] which can hinder the net flow of phonons, thus reducing sound velocity (v_m) and achieving the intrinsic κ_L.

As shown in Fig. 11(a), the binary orthorhombic GeSe embraces the large v_m. In comparison, the metavalently bonded rhombohedral or cubic GeSe-based alloys demonstrate a reduction in v_m, favoring a low κ_L. Figure 11(b) shows the phonons of $(GeSe)_{0.9}(AgBiTe_2)_{0.1}$ and $(GeSe)_{0.9}(AgBiSe_2)_{0.1}$ at Γ point calculated by first-principles density functional perturbation theory (DFPT), and the absence of imaginary frequency indicates their stability.[93,94] Notably, the phonon density-of-states analysis unravels the existence of soft optical modes at frequencies below 50 cm^{-1} [Figs. 11(c) and 11(d)], potentially deriving from the ferroelectric instability in the rhombohedral phase.[93,94] These soft optical phonons coupled with the acoustic phonons enhance the anharmonic scattering of heat-carrying phonons, leading to a significant reduction in κ_L. Furthermore, the lattice anharmonicity is described by the Grüneisen parameter (γ).[41] As shown in Fig. 11(e), a

01 October 2024 06:40:17

Published under an exclusive license by AIP Publishing

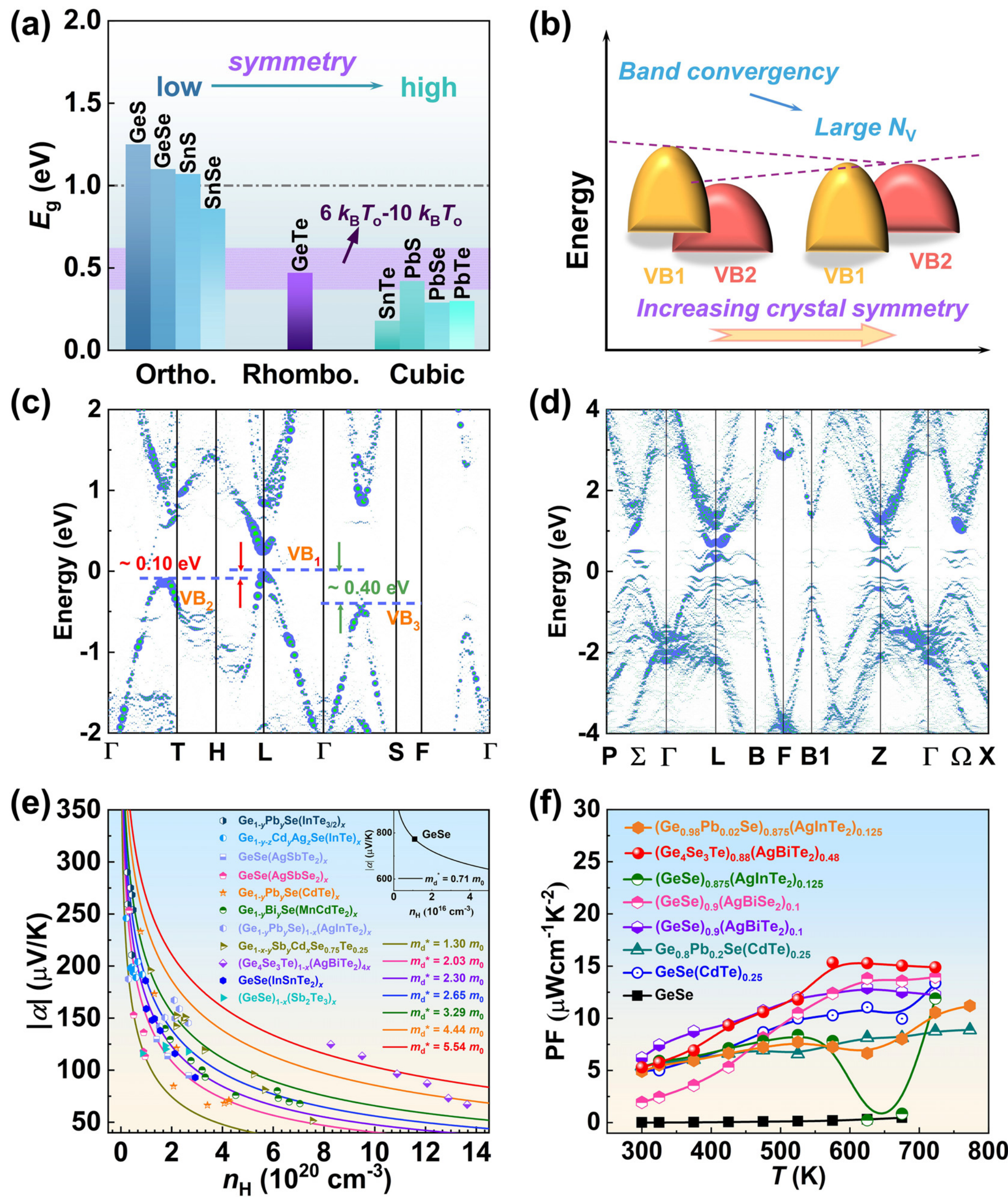

FIG. 10. (a) A summary of bandgap (E_g) of typical binary Group IV–VI compounds with different crystal structures. (b) Schematic diagram showing band convergence. Band structures of (c) rhombohedral $Ge_{21}CdPb_4Se_{22}Te_5$ and (d) rhombohedral $Ge_{21}Ag_3In_3Se_{21}Te_6$. (e) Room-temperature Pisarenko plots of GeSe-based alloys.[91,92,99,100,102–108] (f) Power factor (PF) as a function of temperature of GeSe-based alloys.[93,94,103,104,106] Panel (a) reproduced with permission from Li *et al.*, Nano Energy **100**, 107434 (2022). Copyright 2022 Elsevier.[105] Panel (c) reproduced with permission from Yao *et al.*, The Innovation **4**(6), 100522 (2023). Copyright 2023 Cell Press.[104] Panel (d) reproduced with permission from Huang *et al.*, Interdiscip. Mater. **3**(4), 607–620 (2024). Copyright 2024 Wiley-VCH.[103]

large γ is achieved in several rhombohedral or cubic GeSe-based alloys. In addition, v_m and γ for rhombohedral GeSe-based alloys are comparable to those of advanced MVB materials with excellent TE performance, which is responsible for the low κ_L in high symmetric GeSe-based alloys. Figure 11(f) depicts the temperature dependence of κ_L of typical samples. As shown, the rhombohedral GeSe illustrates a lower κ_L than that of orthorhombic GeSe, especially near room temperatures. For instance, κ_L of the rhombohedral $(Ge_{0.98}Pb_{0.02}Se)_{0.875}(AgInTe_2)_{0.125}$ decreases from $\sim$0.72 to $\sim$0.45 W m^{-1} K^{-1} between room temperature and 773 K, while the orthorhombic GeSe shows the

01 October 2024 06:40:17

Published under an exclusive license by AIP Publishing

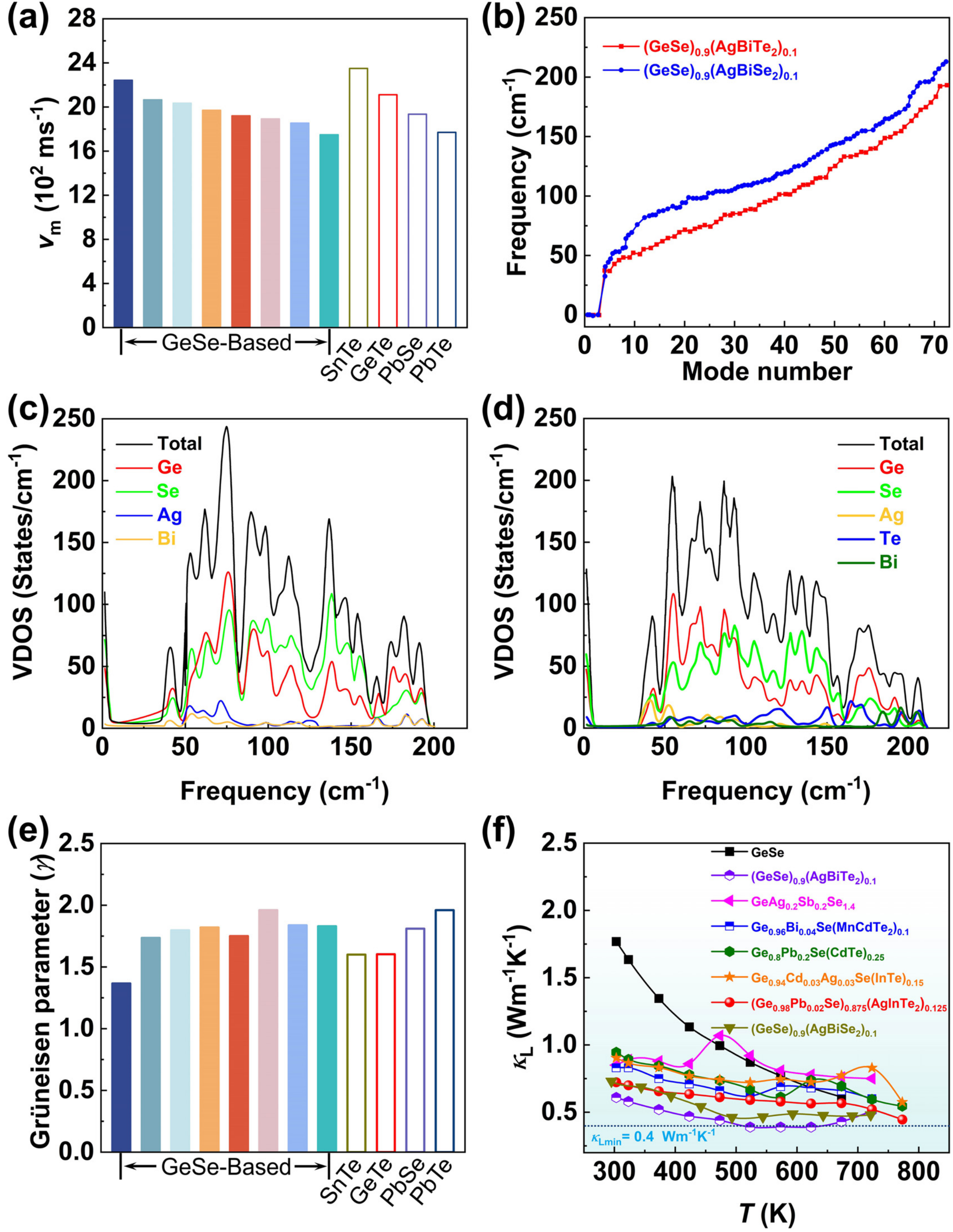

FIG. 11. (a) Mean sound velocity of GeSe-based alloys compared to other Group IV–VI compounds.[97,176–178] GeSe-based materials from left to right are pristine GeSe,[103] $(GeSe)_{0.875}(AgInTe_2)_{0.125}$,[103] $(Ge_{0.98}Pb_{0.02}Se)_{0.875}(AgInTe_2)_{0.125}$,[103] $GeSe(CdTe)_{0.25}$,[104] $(Ge_4Se_3Te)_{0.88}(AgBiTe_2)_{0.48}$,[106] $Ge_{0.55}Bi_{0.2}Pb_{0.25}Se(In_2Te_3)_{0.1}$,[110] $(Ge_{0.7}Bi_{0.3}Se)_{0.7}(AgSnTe_2)_{0.3}$,[109] and $Ge_{0.80}Pb_{0.20}Se(CdTe)_{0.25}$,[104] respectively. (b) Phonon frequencies of $(GeSe)_{0.9}(AgBiSe_2)_{0.1}$ and $(GeSe)_{0.9}(AgBiTe_2)_{0.1}$.[93,94] Projected phonon density-of-states of (c) $(GeSe)_{0.9}(AgBiSe_2)_{0.1}$ and (d) $(GeSe)_{0.9}(AgBiTe_2)_{0.1}$. (e) Grüneisen parameter (γ) of GeSe-based alloys that compared to other Group IV–VI compounds.[97,176–178] (f) Temperature-dependent lattice thermal conductivity (κ_L) of typical GeSe-based alloys.[91,93,94,100,103–105] Panel (c) reproduced with permission from Sarkar *et al.*, J. Am. Chem. Soc. **142**(28), 12237–12244 (2020). Copyright 2020 American Chemical Society.[94] Panel (d) reproduced with permission from Sarkar *et al.*, Angew. Chem., Int. Ed. **60**(18), 10350–10358 (2021). Copyright 2021 Wiley-VCH.[93]

01 October 2024 06:40:17

Published under an exclusive license by AIP Publishing

κ_L of ~1.77 and 0.61 W m^{-1} K^{-1} at room temperature and 673 K, respectively.[103]

B. Ferroelectric domains in rhombohedral GeSe

Rhombohedral GeSe employs the MVB, characterized by a long-range interaction along the ⟨100⟩ direction.[179] Considering the presence of ferroelectricity that derives from the competition of long- and short-range interactions in rhombohedral GeSe, an exclusive ferroelectric domain (herringbone structure) should serve as the scattering center for further phonon scattering, similar to that observed in rhombohedral GeTe.[180,181] For example, the high density of nanoscale domain structures with strip contrast is observed in $Ge_{0.96}Bi_{0.04}Se(MnCdTe_2)_{0.1}$ through scanning transmission electron microscopy (STEM) and high-angle annular dark-field (HAADF) analysis, as shown in Figs. 12(a) and 12(d).[105] The atomic resolution HAADF image and selected area electron diffraction (SAED) pattern affirm the rhombohedral structure of $Ge_{0.96}Bi_{0.04}Se(MnCdTe_2)_{0.1}$ [Figs. 12(b) and 12(c)]. To gain an insight into the structure of these domains, Fig. 12(e) presents the atomic resolution STEM-HAADF image extracted from the white frame in the enlarged domain area as shown in Fig. 12(d), revealing small-angle grain boundaries with an angle of approximately 3.82° [Fig. 12(f)].[105] The ferroelectric domains and the small-angle grain boundaries can significantly scatter phonons and reduce κ_L.

The ferroelectricity is also demonstrated in rhombohedral $(GeSe)_{0.9}(AgBiTe_2)_{0.1}$ by piezo-response force microscopy (PFM) and spectroscopy analysis.[93] As shown in Figs. 12(g) and 12(h), the topographic and phase images reveal the existence of distinct local ferroelectric domains displaying consistent electrical polarization.

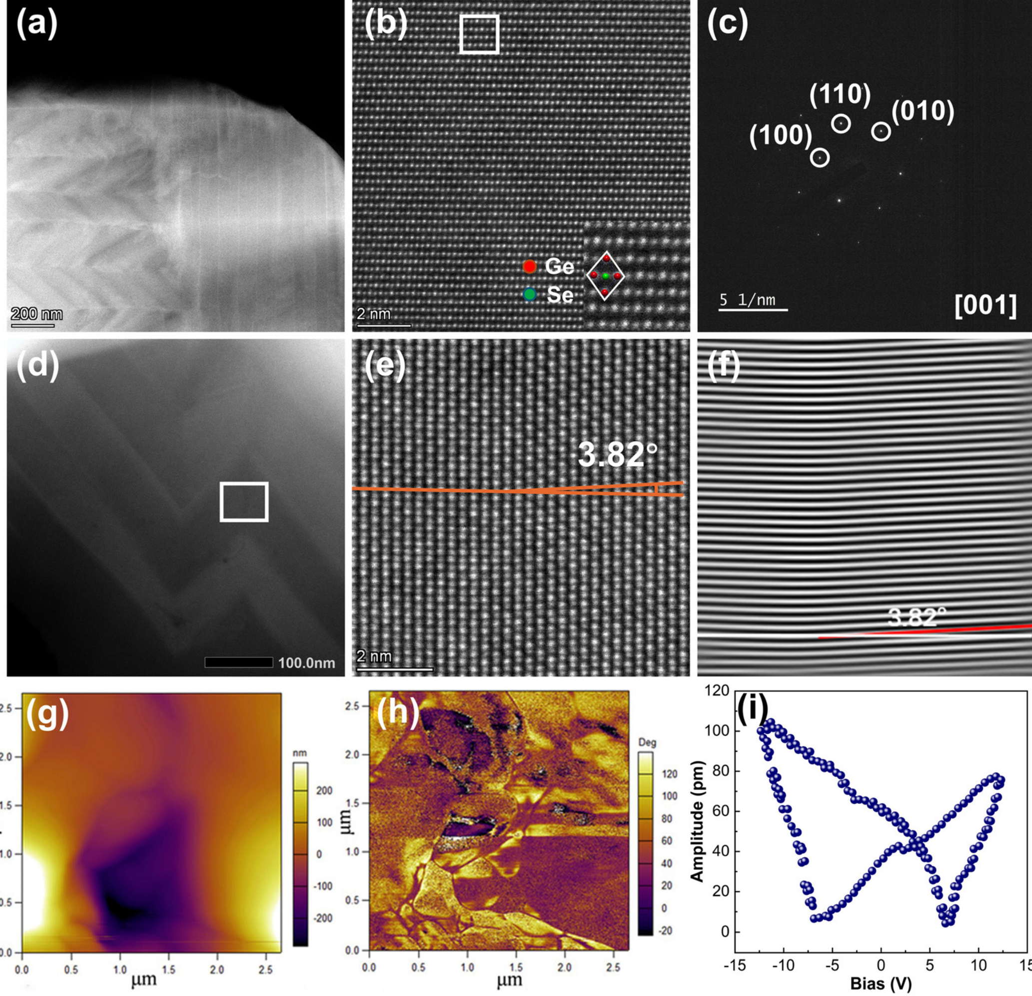

FIG. 12. (a) High-angle annular dark-field scanning transmission electron microscopy (HAADF-STEM) image of $Ge_{0.96}Bi_{0.04}Se(MnCdTe_2)_{0.1}$. (b) Atom resolution HAADF image and (c) selected area electron diffraction pattern along [001] direction. (d) and (e) HAADF images of domain walls and (f) image using Fourier filtering with reflections of (1–10). (g) Topography and (h) phase images of $(GeSe)_{0.9}(AgBiTe_2)_{0.1}$. (i) Amplitude of switching piezo-response force microscopy (PFM) spectroscopy analysis for $(GeSe)_{0.9}(AgBiTe_2)_{0.1}$. Panels (a)–(f) reproduced with permission from Li *et al.*, Nano Energy **100**, 107434 (2022). Copyright 2022 Elsevier.[105] Panels (g)–(i) reproduced with permission from Sarkar *et al.*, Angew. Chem., Int. Ed. **60**(18), 10350–10358 (2021). Copyright 2021 Wiley-VCH.[93]

01 October 2024 06:40:17

Published under an exclusive license by AIP Publishing

Additionally, the butterfly-shaped pattern evident in the amplitude of the PFM response signal provides additional evidence of the existence of local ferroelectric domains within the rhombohedral $(GeSe)_{0.9}(AgBiSe_2)_{0.1}$, as illustrated in Fig. 12(i). These ferroelectric domains in the rhombohedral phase effectively impede phonon transport, leading to a significantly reduced κ_L.

C. Phonon scattering via extra-scattering mechanisms

The multiple scale lattice defects serve as additional phonon scattering centers, effectively inhibiting the phonon transport across a wide frequency range, consequently leading to significant suppression of κ_L. The conventional lattice defects in GeSe mainly include the point defects, grain boundaries, as well as precipitates, as schematically depicted in Fig. 13(a). For a comprehensive understanding of the impact of phonon scattering center on the κ_L, the spectral lattice thermal conductivity (κ_s) with respect to the wavelength has been calculated using Debye Callaway model by considering the Umklapp processes scattering (U), boundary scattering (B), point defect scattering (PD), and precipitate scattering (P).[104] Since the integral of κ_s can be defined as κ_L, the region between per two curves depicts the reduction in κ_L caused by the corresponding scattering source. As shown in Fig. 13(b), the point defects mainly scatter high-frequency phonons, while precipitates and boundaries contribute to phonon scattering in mid- to low-frequency and low-frequency ranges, respectively.

The point defects and boundaries are commonly found in doped samples, especially in rhombohedral or cubic GeSe, which are generally formed by multi-component alloying.[99,103,108] Furthermore, the incorporation of precipitates serves as additional lattice defects, which further enhances phonon scattering. In the case of rhombohedral $Ge_{0.8}Pb_{0.2}Se(CdTe)_{0.25}$, high-resolution transmission electron microscopy (HRTEM) characterization reveals the existence of sub micrometer-scale CdSe precipitates in this sample, along with the phase boundaries between the precipitate and matrix, as depicted in Figs. 13(c)–13(e).[104] Figure 13(f) presents a summarized diagram of κ_L reported in GeSe-based TE materials, suggesting that much lower κ_L values are achieved in rhombohedral and cubic GeSe. For example, a reduced κ_L of 0.55 W m^{-1} K^{-1} at 773 K is achieved in rhombohedral $Ge_{0.80}Pb_{0.20}Se(CdTe)_{0.25}$, primarily originating from the strong anharmonicity and the introduction of impurity and point defect scattering.[104] Furthermore, a reduction in κ_L is also observed in cubic GeSe, reaching 0.55 W m^{-1} K^{-1} at 523 K for $GeSeTe_{0.15}(InSnTe_2)_{0.2}$[108] and 0.83 W m^{-1} K^{-1} at 710 K for $(GeSe)_{0.92}(Sb_2Te_3)_{0.08}$.[107]

VII. COMPOSITE PHASE ENGINEERING

Composite engineering enables the simultaneous tuning of carrier and phonon transport, thereby favoring overall TE performance.[182] As a representative example in GeSe, a composite phase combining both orthorhombic and rhombohedral structures is achieved through InTe alloying.[100] Given that these phase structures are characterized by distinct chemical bonding mechanisms, further investigation into the formation of dual phases is conducted through atom probe tomography (APT) measurements. As shown in Fig. 14(a), the 3D reconstruction of the $GeSe(InTe)_{0.15}$ sample illustrates the distribution of Ge, Se, In, and Te, revealing iso-composition surfaces rich in Te and Ge (indicated by different colors). Figure 14(b) displays the corresponding 3D proximity histogram map, exhibiting PME values for different regions. Specifically, the bottom region with a high PME represents the utilization of MVB, indicative of the dominant rhombohedral phase. The top-left area shows a low PME value corresponding to the orthorhombic phase, while the low PME value of the top-right region is caused by Ge- and In-rich areas.

To explore the microstructures of the orthorhombic and rhombohedral GeSe composite, Fig. 14(c) presents a characteristic TEM image, revealing two sets of areas with a conspicuous interface. Select area electron diffraction (SAED) is conducted to identify the diffraction patterns and, thereby, the phase structures. The diffraction patterns of the two different contrast areas as shown in Figs. 14(d) and 14(e) correspond to orthorhombic GeSe along the [001] direction and rhombohedral GeSe along the $[\bar{1}01]$ direction, respectively. The HRTEM image in Fig. 14(f) further exhibits the different phase contrast of rhombohedral and orthorhombic structures, which are separated by the interface. The inverse fast Fourier transformation (IFFT) analysis [Fig. 14(g)] reveals a coherent interface without significant strains [Fig. 14(h)]. The dual-phase composite leads to the simultaneous increase in n_H, μ_H, and m_d^*, as well as the strong interfacial phonon scattering originates from the phonon mismatch between the two phases given the different chemical bonding mechanisms. These collectively enhance zT value via synergistic tuning of electrical and thermal transport behavior.

VIII. MECHANICAL PERFORMANCE AND ENERGY-CONVERSION EFFICIENCY

In addition to optimizing TE performance, mechanical robustness plays a pivotal role in the development of excellent TE materials. A robust mechanical performance guarantees steady operation, contributing to the long-term service life of TE devices. The Vickers hardness and compression strength are key criteria to evaluate mechanical performance. The pristine GeSe exhibits a similar Vickers hardness compared to pristine GeTe but surpasses pristine PbTe. Through the regulation of crystal structure and microstructure, a remarkable increase in Vickers hardness is achieved in GeSe,[100,105] surpassing GeTe-based materials and other systems such as Bi_2Te_3 and PbTe.[151] Additionally, element doping significantly enhances the initially inferior compression strength in pristine GeSe.[100] These findings collectively highlight the promising prospects of GeSe in TE applications.

However, standing as an emerging TE system that has been investigated in recent years, reports on GeSe-based TE devices are currently lacking. In this vein, GeSe alloying with $AgInTe_2$ and Pb achieved an enhanced zT value of 1.0 at 773 K. Consequently, a single-leg GeSe-based TE device was successfully fabricated using this sample, showing a maximum η of 4.90%, and a power density of 1.12 W cm^{-2} under a temperature dependence of 500 K.[103] This remains the only report on GeSe-based TE devices to date. In addition, the theoretical prediction of their η based on the currently achieved state-of-the-art zT value suggests that GeSe exhibits a relatively high η. Therefore, the exploration of strategies aiming at further enhancing TE performance becomes imperative for the development of advanced GeSe-based materials.

IX. SUMMARY AND OUTLOOK

As a burgeoning thermoelectric material, binary orthorhombic GeSe exhibits an ultralow figure of merit zT, attributed to intrinsic factors, such as the large energy bandgap, low carrier concentration, and limited carrier mobility. Traditional chemical doping methods fall short of significantly increasing carrier concentration due to their low

01 October 2024 06:40:17

Published under an exclusive license by AIP Publishing

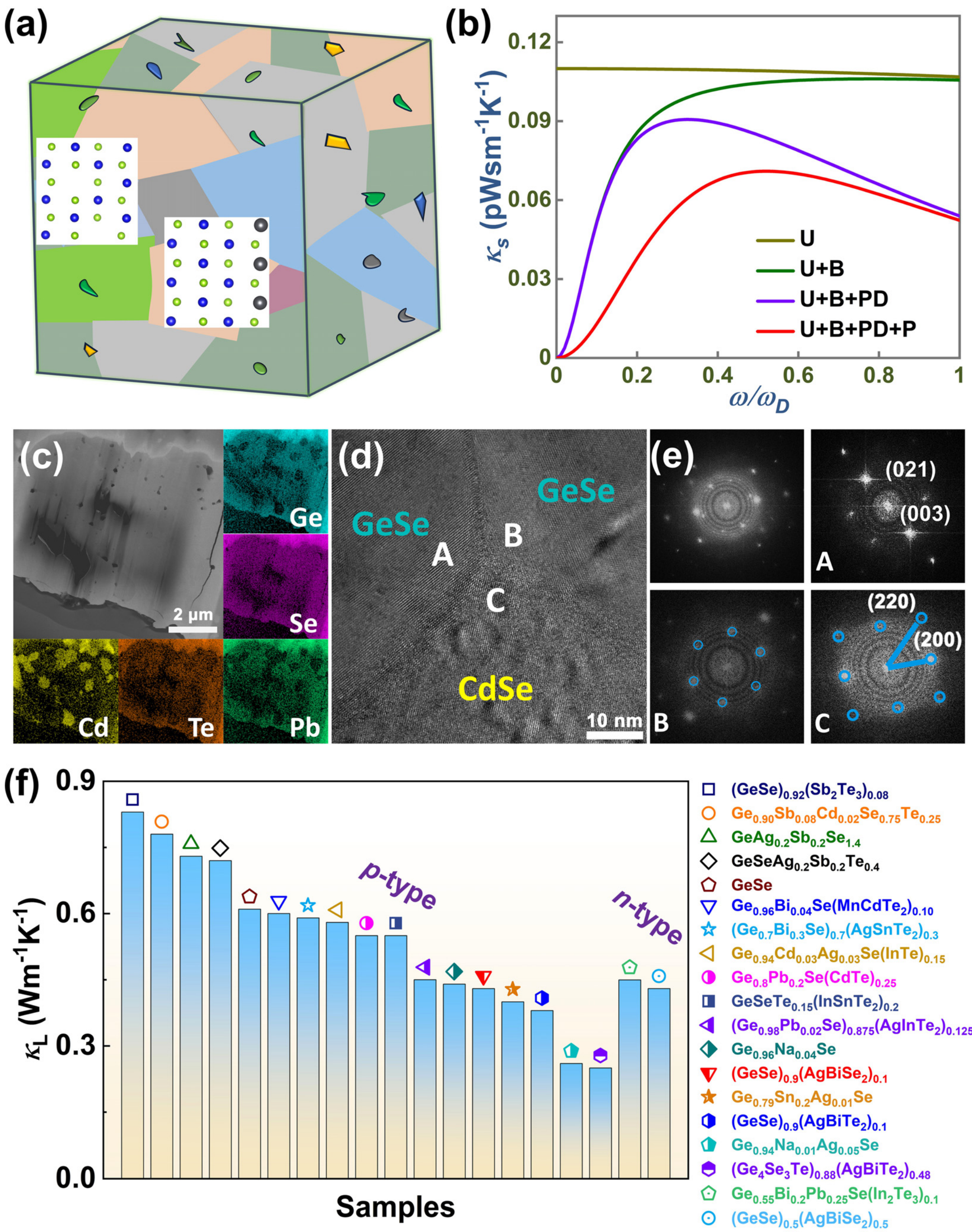

FIG. 13. (a) Schematic diagram of the incorporation of point defects, grain boundaries, and precipitations in the sintered bulk GeSe. (b) Calculated spectral lattice thermal conductivity (κ_S) with respect to the frequency (ω) using the Debye–Callaway model by considering several scattering mechanisms. (c)–(e) Transmission electron microscopy (TEM) image intuitively exhibits the precipitations and boundaries. (f) A summary of minimum lattice thermal conductivity (κ_L) of GeSe-based TE materials.[87–89,91–94,99,100,103–111] Panels (b)–(e) reproduced with permission from Yao *et al.*, The Innovation **4**(6), 100522 (2023). Copyright 2023 Cell Press.[104]

solubility. However, GeSe possesses three inherent crystal structures of orthorhombic, rhombohedral, and cubic phases, each determined by different chemical bonding mechanism. The tailoring of chemical bonding mechanism from covalent bonding to metavalent bonding and consequently the phase transition from orthorhombic to rhombohedral and cubic provides extra-degrees of freedom to enhance the zT value of GeSe-based materials. Specifically, the rhombohedral and cubic GeSe embrace advantages such as small formation energy of Ge

01 October 2024 06:40:17

Published under an exclusive license by AIP Publishing

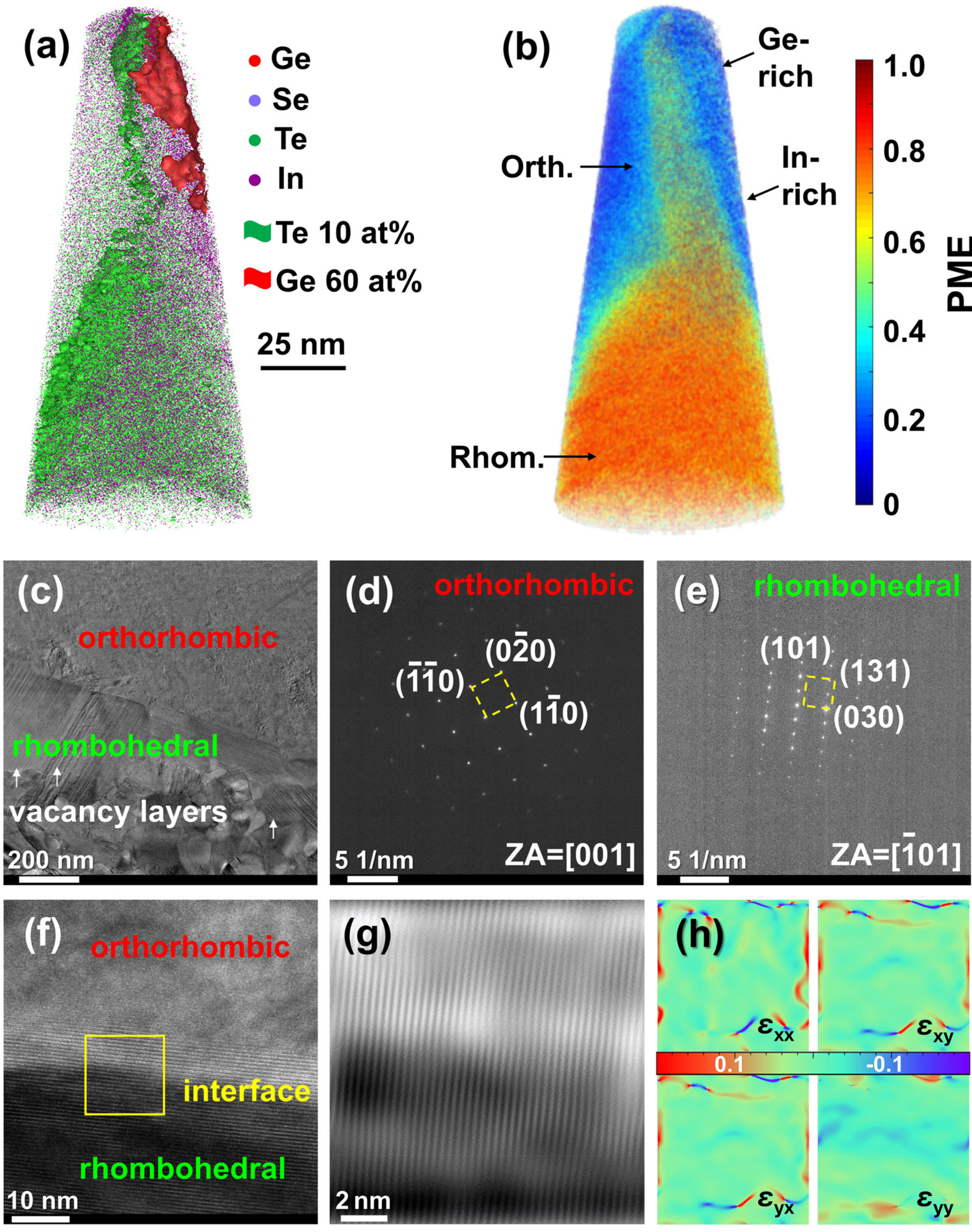

FIG. 14. Atom probe tomography (APT) measurement and TEM characterization of $GeSe(InTe)_{0.15}$ illustrating the chemical compositions and chemical bonding mechanisms in the dual phases GeSe. (a) Three-dimensional (3D) map exhibiting the distribution of elements. (b) 3D probability of multiple events (PME) map showcasing the different PME values for different regions. (c) TEM image shows the different phases with different contrasts. Select area electron diffraction patterns of the (d) upper part and (e) middle part of figure (c). (f) The interface between the rhombohedral and orthorhombic phases. (g) Inverse fast Fourier transformation of the interface taken from the yellow frame of figure (f), indicating the coherent feature. (h) Strain analysis via geometric phase analysis (GPA). Reproduced with permission from Hu *et al.*, Adv. Funct. Mater. **33**(17), 2214854 (2023). Copyright 2023 Wiley-VCH.[100]

vacancy, large band degeneracy, multiple valence band convergence, as well as the metavalent bonding featuring weak chemical bonds and strong anharmonicity, favoring the enhanced carrier concentration, large density-of-state effective mass, and strong phonon–phonon interactions. Combined with the abundant lattice defects for phonon scattering across a broad wavelength range, the high-symmetry phases yield a significantly increased zT exceeding 1.0, surpassing those of pristine orthorhombic GeSe. These concepts for zT enhancement of

01 October 2024 06:40:17

Published under an exclusive license by AIP Publishing

GeSe can also be applied to improve the TE performance of other phase change materials.

Future research on GeSe may encompass the following aspects:

(1) Enhancing carrier mobility to improve electrical conductivity. Increasing carrier mobility is essential for optimizing electrical conductivity, a key parameter for thermoelectric performance. Despite phase manipulation optimizing valence band edge structures, the resultant carrier mobility only reaches about 10–15 $cm^2 V^{-1} s^{-1}$, lower than that of TE materials with high zT value.
(2) Exploiting the high thermoelectric performance of n-type GeSe materials. Achieving commercially viable thermoelectric devices involves combining p-type and n-type legs with similar chemical compositions. While existing research predominantly concentrates on p-type GeSe, attention to the n-type counterpart remains limited, hindering the development of GeSe-based thermoelectric devices.
(3) Screening interface materials for GeSe-based thermoelectric devices. Currently, there is an absence of research on GeSe-based devices. Identifying suitable interface materials is crucial for minimizing energy loss between the thermoelectric material and electrode material during electrical and heat transport. Conversely, the diffusion of elements or chemical reactions could significantly impact the lifetime and energy-conversion efficiency of a thermoelectric device.

ACKNOWLEDGMENTS

The work was supported by the National Natural Science Foundation of China (52071218), the National Key R&D Program of China (2021YFB1507403), the Shenzhen Science and Technology Innovation Commission (JCYJ20230808105700001), and the Shenzhen University 2035 Program for Excellent Research (00000218). M.H. acknowledges funding from Australian Research Council (FT230100316). L.C. and M.H. acknowledge funding from Trailblazer Universities program iLAuNCH.

AUTHOR DECLARATIONS

Conflict of Interest

The authors have no conflicts to disclose.

Author Contributions

Tu Lyu: Formal analysis (equal); Resources (equal); Validation (equal); Visualization (equal); Writing – original draft (equal). **Moran Wang:** Resources (equal); Visualization (equal). **Xiaohuan Luo:** Data curation (equal); Formal analysis (equal); Methodology (equal); Validation (equal). **Yuwei Zhou:** Data curation (equal); Methodology (equal); Resources (equal); Visualization (equal). **Lei Chen:** Investigation (equal); Validation (equal); Writing – review & editing (equal). **Min Hong:** Conceptualization (equal); Formal analysis (equal); Supervision (equal); Writing – review & editing (equal). **Lipeng Hu:** Methodology (equal); Project administration (equal); Resources (equal); Supervision (equal); Writing – original draft (equal); Writing – review & editing (equal).

DATA AVAILABILITY

Data sharing is not applicable to this article as no new data were created or analyzed in this study.

REFERENCES

[1]X.-L. Shi, J. Zou, and Z.-G. Chen, Chem. Rev. **120**(15), 7399–7515 (2020).
[2]B. Jiang, Y. Yu, J. Cui, X. Liu, L. Xie, J. Liao, Q. Zhang, Y. Huang, S. Ning, B. Jia, B. Zhu, S. Bai, L. Chen, J. Pennycook Stephen, and J. He, Science **371**(6531), 830–834 (2021).
[3]Z. Li, C. Xiao, and Y. Xie, Appl. Phys. Rev. **9**(1), 011303 (2022).
[4]P. Li, P. Qiu, Q. Xu, J. Luo, Y. Xiong, J. Xiao, N. Aryal, Q. Li, L. Chen, and X. Shi, Nat. Commun. **13**(1), 7612 (2022).
[5]W. Liu, K. Yin, Q. Zhang, C. Uher, and X. Tang, Natl. Sci. Rev. **4**(4), 611–626 (2017).
[6]T. Zhu, Y. Liu, C. Fu, J. P. Heremans, J. G. Snyder, and X. Zhao, Adv. Mater. **29**(14), 1605884 (2017).
[7]M. Hong, J. Zou, and Z.-G. Chen, Adv. Mater. **31**(14), 1807071 (2019).
[8]J. Mao, G. Chen, and Z. Ren, Nat. Mater. **20**(4), 454–461 (2021).
[9]J. He and T. M. Tritt, Science **357**(6358), eaak9997 (2017).
[10]T. M. Tritt and M. A. Subramanian, MRS Bull. **31**(3), 188–198 (2006).
[11]J. Yang and T. Caillat, MRS Bull. **31**(3), 224–229 (2006).
[12]R. He, G. Schierning, and K. Nielsch, Adv. Mater. Technol. **3**(4), 1700256 (2018).
[13]I. Chowdhury, R. Prasher, K. Lofgreen, G. Chrysler, S. Narasimhan, R. Mahajan, D. Koester, R. Alley, and R. Venkatasubramanian, Nat. Nanotechnol. **4**(4), 235–238 (2009).
[14]W.-Y. Chen, X.-L. Shi, J. Zou, and Z.-G. Chen, Mater. Sci. Eng., R **151**, 100700 (2022).
[15]D. Yang, Y. Xing, J. Wang, K. Hu, Y. Xiao, K. Tang, J. Lyu, J. Li, Y. Liu, P. Zhou, Y. Yu, Y. Yan, and X. Tang, Interdiscip. Mater. **3**(2), 326–337 (2024).
[16]Q. Yan and M. G. Kanatzidis, Nat. Mater. **21**(5), 503–513 (2022).
[17]X. Tang, Z. Li, W. Liu, Q. Zhang, and C. Uher, Interdiscip. Mater. **1**(1), 88–115 (2022).
[18]Y. Luo, J. Wang, J. Yang, D. Mao, J. Cui, B. Jia, X. Liu, K. Nielsch, X. Xu, and J. He, Energy Environ. Sci. **16**(9), 3743–3752 (2023).
[19]S. Xu, M. Hong, M. Li, Q. Sun, Y. Yin, W. Liu, X. Shi, M. Dargusch, J. Zou, and Z.-G. Chen, Appl. Phys. Rev. **8**(4), 041404 (2021).
[20]Z. Bu, X. Zhang, Y. Hu, Z. Chen, S. Lin, W. Li, C. Xiao, and Y. Pei, Nat. Commun. **13**(1), 237 (2022).
[21]K. Shen, Q. Yang, P. Qiu, Z. Zhou, S. Yang, T.-R. Wei, and X. Shi, Adv. Mater. **36**, 2407424 (2024).
[22]M. Tan, W.-D. Liu, X.-L. Shi, Q. Sun, and Z.-G. Chen, Appl. Phys. Rev. **10**(2), 021404 (2023).
[23]Z. Liu, T. Hong, L. Xu, S. Wang, X. Gao, C. Chang, X. Ding, Y. Xiao, and L.-D. Zhao, Interdiscip. Mater. **2**(1), 161–170 (2023).
[24]L. Xie, J. Yang, Z. Liu, N. Qu, X. Dong, J. Zhu, W. Shi, H. Wu, G. Peng, F. Guo, Y. Zhang, W. Cai, H. Wu, H. Zhu, H. Zhao, Z. Liu, and J. Sui, Mater. Today **65**, 5–13 (2023).
[25]H. Xie, L.-D. Zhao, and M. G. Kanatzidis, Interdiscip. Mater. **3**(1), 5–28 (2024).
[26]L. Hu, F. Meng, Y. Zhou, J. Li, A. Benton, J. Li, F. Liu, C. Zhang, H. Xie, and J. He, Adv. Funct. Mater. **30**(45), 2005202 (2020).
[27]H.-L. Zhuang, H. Hu, J. Pei, B. Su, J.-W. Li, Y. Jiang, Z. Han, and J.-F. Li, Energy Environ. Sci. **15**(5), 2039–2048 (2022).
[28]T. Lyu, Q. Yang, Z. Li, C. Zhang, F. Liu, J. Li, L. Hu, and G. Xu, ACS Appl. Mater. Interfaces **15**(15), 19250–19257 (2023).
[29]D. Su, J. Cheng, S. Li, S. Zhang, T. Lyu, C. Zhang, J. Li, F. Liu, and L. Hu, J. Mater. Sci. Technol. **138**, 50–58 (2023).
[30]B. Zhu, X. Liu, Q. Wang, Y. Qiu, Z. Shu, Z. Guo, Y. Tong, J. Cui, M. Gu, and J. He, Energy Environ. Sci. **13**(7), 2106–2114 (2020).
[31]M. Zhang, Z. Gao, Q. Lou, Q. Zhu, J. Wang, Z. Han, C. Fu, and T. Zhu, Adv. Funct. Mater. **34**(6), 2307864 (2024).
[32]F. Li, X. Liu, S.-R. Li, X.-F. Zhang, N. Ma, X.-J. Li, X.-Y. Lin, L. Chen, H. Wu, and L.-M. Wu, Energy Environ. Sci. **17**(1), 158–172 (2024).

01 October 2024 06:40:17

Published under an exclusive license by AIP Publishing

[33]B. Jia, Y. Huang, Y. Wang, Y. Zhou, X. Zhao, S. Ning, X. Xu, P. Lin, Z. Chen, B. Jiang, and J. He, Energy Environ. Sci. **15**(5), 1920–1929 (2022).
[34]L. Su, D. Wang, S. Wang, B. Qin, Y. Wang, Y. Qin, Y. Jin, C. Chang, and L.-D. Zhao, Science **375**(6587), 1385–1389 (2022).
[35]B. Jia, D. Wu, L. Xie, W. Wang, T. Yu, S. Li, Y. Wang, Y. Xu, B. Jiang, Z. Chen, Y. Weng, and J. He, Science **384**(6691), 81–86 (2024).
[36]Y. Qin, B. Qin, T. Hong, X. Zhang, D. Wang, D. Liu, Z.-Y. Wang, L. Su, S. Wang, X. Gao, Z.-H. Ge, and L.-D. Zhao, Science **383**(6688), 1204–1209 (2024).
[37]J. Zhong, X. Yang, T. Lyu, G. Liang, S. Zhang, C. Zhang, W. Ao, F. Liu, P. Nan, B. Ge, and L. Hu, Sci. Bull. **69**(8), 1037–1049 (2024).
[38]Z. Liu, W. Gao, H. Oshima, K. Nagase, C.-H. Lee, and T. Mori, Nat. Commun. **13**(1), 1120 (2022).
[39]Z. Liu, N. Sato, W. Gao, K. Yubuta, N. Kawamoto, M. Mitome, K. Kurashima, Y. Owada, K. Nagase, C.-H. Lee, J. Yi, K. Tsuchiya, and T. Mori, Joule **5**(5), 1196–1208 (2021).
[40]S. Han, S. Dai, J. Ma, Q. Ren, C. Hu, Z. Gao, M. Duc Le, D. Sheptyakov, P. Miao, S. Torii, T. Kamiyama, C. Felser, J. Yang, C. Fu, and T. Zhu, Nat. Phys. **19**(11), 1649–1657 (2023).
[41]J. Zhu, L. Xie, Z. Ti, J. Li, M. Guo, X. Zhang, P.-F. Liu, L. Tao, Z. Liu, Y. Zhang, and J. Sui, Appl. Phys. Rev. **10**(3), 031405 (2023).
[42]X. Ai, B. Lei, M. O. Cichocka, L. Giebeler, R. B. Villoro, S. Zhang, C. Scheu, N. Pérez, Q. Zhang, A. Sotnikov, D. J. Singh, K. Nielsch, and R. He, Adv. Funct. Mater. **33**(48), 2305582 (2023).
[43]X. W. Wang, H. Lee, Y. C. Lan, G. H. Zhu, G. Joshi, D. Z. Wang, J. Yang, A. J. Muto, M. Y. Tang, J. Klatsky, S. Song, M. S. Dresselhaus, G. Chen, and Z. F. Ren, Appl. Phys. Lett. **93**(19), 193121 (2008).
[44]G. Joshi, H. Lee, Y. Lan, X. Wang, G. Zhu, D. Wang, R. W. Gould, D. C. Cuff, M. Y. Tang, M. S. Dresselhaus, G. Chen, and Z. Ren, Nano Lett. **8**(12), 4670–4674 (2008).
[45]J. Yang, B. Lu, R. Song, H. Hou, L. Zhao, X. Zhang, G. Liu, and G. Qiao, J. Eur. Ceram. Soc. **42**(1), 169–174 (2022).
[46]B. Yu, M. Zebarjadi, H. Wang, K. Lukas, H. Wang, D. Wang, C. Opeil, M. Dresselhaus, G. Chen, and Z. Ren, Nano Lett. **12**(4), 2077–2082 (2012).
[47]Y.-L. Pei, H. Wu, D. Wu, F. Zheng, and J. He, J. Am. Chem. Soc. **136**(39), 13902–13908 (2014).
[48]Z.-Z. Luo, S. Cai, S. Hao, T. P. Bailey, I. Spanopoulos, Y. Luo, J. Xu, C. Uher, C. Wolverton, V. P. Dravid, Q. Yan, and M. G. Kanatzidis, Angew. Chem., Int. Ed. **60**(1), 268–273 (2021).
[49]J. Dong, F.-H. Sun, H. Tang, J. Pei, H.-L. Zhuang, H.-H. Hu, B.-P. Zhang, Y. Pan, and J.-F. Li, Energy Environ. Sci. **12**(4), 1396–1403 (2019).
[50]S. Zulkifal, Z. Wang, X. Zhang, S. Siddique, Y. Yu, C. Wang, Y. Gong, S. Li, D. Li, Y. Zhang, P. Wang, and G. Tang, Adv. Sci. **10**(17), 2206342 (2023).
[51]Q. Zhang, B. Liao, Y. Lan, K. Lukas, W. Liu, K. Esfarjani, C. Opeil, D. Broido, G. Chen, and Z. Ren, Proc. Natl. Acad. Sci. U. S. A. **110**(33), 13261–13266 (2013).
[52]J. P. Heremans, B. Wiendlocha, and A. M. Chamoire, Energy Environ. Sci. **5**(2), 5510–5530 (2012).
[53]J. Sun, C. Xie, W. Cui, F. Yan, J. Li, J. Zhang, X. Sang, X. Tang, and G. Tan, Chem. Mater. **35**(11), 4366–4374 (2023).
[54]Y. Z. Li, Q. Zhang, K. Liu, Y. J. Lin, N. Lin, Y. Yu, F. Liu, X. B. Zhao, B. H. Ge, O. Cojocaru-Mirédin, C. G. Fu, and T. J. Zhu, Mater. Today Nano **22**, 100340 (2023).
[55]J. H. Cheng, T. Lyu, G. G. Liang, W. Q. Yao, W. Q. Ao, C. H. Zhang, J. Q. Li, F. S. Liu, and L. P. Hu, Mater. Today Phys. **27**, 100820 (2022).
[56]B. Qin, D. Wang, and L.-D. Zhao, InfoMat **3**(7), 755–789 (2021).
[57]J. Tang, B. Gao, S. Lin, X. Wang, X. Zhang, F. Xiong, W. Li, Y. Chen, and Y. Pei, ACS Energy Lett. **3**(8), 1969–1974 (2018).
[58]M. Wang, M. Hong, X. Fang, J. Cheng, T. Lyu, Y. Zhou, X. Luo, C. Zhang, W. Ao, F. Liu, and L. Hu, Acta Mater. **266**, 119675 (2024).
[59]L.-C. Yin, W.-D. Liu, M. Li, D.-Z. Wang, H. Wu, Y. Wang, L. Zhang, X.-L. Shi, Q. Liu, and Z.-G. Chen, Adv. Funct. Mater. **33**(25), 2301750 (2023).
[60]G. Tan, W. G. Zeier, F. Shi, P. Wang, G. J. Snyder, V. P. Dravid, and M. G. Kanatzidis, Chem. Mater. **27**(22), 7801–7811 (2015).
[61]G. Tan, F. Shi, S. Hao, H. Chi, T. P. Bailey, L.-D. Zhao, C. Uher, C. Wolverton, V. P. Dravid, and M. G. Kanatzidis, J. Am. Chem. Soc. **137**(35), 11507–11516 (2015).
[62]C. Wang, Y. Gong, W. Xiong, X. Yang, Q. Zhang, Y. Liu, S. Li, X. Huang, D. Li, D. Zhang, P. Nan, B. Ge, and G. Tang, Chem. Mater. **35**(1), 327–336 (2023).
[63]Z. Chen, Z. Jian, W. Li, Y. Chang, B. Ge, R. Hanus, J. Yang, Y. Chen, M. Huang, G. J. Snyder, and Y. Pei, Adv. Mater. **29**(23), 1606768 (2017).
[64]M. Hong, Y. Wang, W. Liu, S. Matsumura, H. Wang, J. Zou, and Z.-G. Chen, Adv. Energy Mater. **8**(30), 1801837 (2018).
[65]Q. Zhou, X. Tan, Q. Zhang, R. Wang, Z. Guo, J. Cai, J. Ye, G. Liu, and J. Jiang, ACS Appl. Mater. Interfaces **14**(40), 45621–45627 (2022).
[66]J. Li, Q. Tan, J.-F. Li, D.-W. Liu, F. Li, Z.-Y. Li, M. Zou, and K. Wang, Adv. Funct. Mater. **23**(35), 4317–4323 (2013).
[67]G. Tan, L.-D. Zhao, and M. G. Kanatzidis, Chem. Rev. **116**(19), 12123–12149 (2016).
[68]R. Wu, Y. Yu, S. Jia, C. Zhou, O. Cojocaru-Mirédin, and M. Wuttig, Nat. Commun. **14**(1), 719 (2023).
[69]Y. Zhu, D. Wang, T. Hong, L. Hu, T. Ina, S. Zhan, B. Qin, H. Shi, L. Su, X. Gao, and L.-D. Zhao, Nat. Commun. **13**(1), 4179 (2022).
[70]S. Liu, Y. Wen, S. Bai, H. Shi, Y. Qin, B. Qin, D. Liu, Q. Cao, X. Gao, L. Su, C. Chang, X. Zhang, and L.-D. Zhao, Adv. Mater. **36**(25), 2401828 (2024).
[71]Z.-Z. Luo, S. Cai, S. Hao, T. P. Bailey, Y. Luo, W. Luo, Y. Yu, C. Uher, C. Wolverton, V. P. Dravid, Z. Zou, Q. Yan, and M. G. Kanatzidis, Energy Environ. Sci. **15**(1), 368–375 (2022).
[72]Z. Chen, H.-H. Cui, S. Hao, Y. Liu, H. Liu, J. Zhou, Y. Yu, Q. Yan, C. Wolverton, V. P. Dravid, Z.-Z. Luo, Z. Zou, and M. G. Kanatzidis, Energy Environ. Sci. **16**(4), 1676–1684 (2023).
[73]W. Liu, L. Xu, Y. Xiao, and L.-D. Zhao, Chem. Eng. J. **465**, 142785 (2023).
[74]B. Jiang, W. Wang, S. Liu, Y. Wang, C. Wang, Y. Chen, L. Xie, M. Huang, and J. He, Science **377**(6602), 208–213 (2022).
[75]M. Hong, Y. Wang, T. Feng, Q. Sun, S. Xu, S. Matsumura, S. T. Pantelides, J. Zou, and Z.-G. Chen, J. Am. Chem. Soc. **141**(4), 1742–1748 (2019).
[76]X. Zhang, Z. Bu, S. Lin, Z. Chen, W. Li, and Y. Pei, Joule **4**(5), 986–1003 (2020).
[77]G. Liang, T. Lyu, L. Hu, W. Qu, S. Zhi, J. Li, Y. Zhang, J. He, J. Li, F. Liu, C. Zhang, W. Ao, H. Xie, and H. Wu, ACS Appl. Mater. Interfaces **13**(39), 47081–47089 (2021).
[78]Y. Liu, X. Zhang, P. Nan, B. Zou, Q. Zhang, Y. Hou, S. Li, Y. Gong, Q. Liu, B. Ge, O. Cojocaru-Mirédin, Y. Yu, Y. Zhang, G. Chen, M. Wuttig, and G. Tang, Adv. Funct. Mater. **32**(47), 2209980 (2022).
[79]T. Lyu, Q. Yang, F. Meng, J. He, A. Benton, C. Chronister, Z. Li, and G. Xu, Chem. Eng. J. **404**, 126925 (2021).
[80]D. Liu, D. Wang, T. Hong, Z. Wang, Y. Wang, Y. Qin, L. Su, T. Yang, X. Gao, Z. Ge, B. Qin, and L.-D. Zhao, Science **380**(6647), 841–846 (2023).
[81]C. Zhou, Y. K. Lee, Y. Yu, S. Byun, Z.-Z. Luo, H. Lee, B. Ge, Y.-L. Lee, X. Chen, J. Y. Lee, O. Cojocaru-Mirédin, H. Chang, J. Im, S.-P. Cho, M. Wuttig, V. P. Dravid, M. G. Kanatzidis, and I. Chung, Nat. Mater. **20**(10), 1378–1384 (2021).
[82]B. Qin, D. Wang, X. Liu, Y. Qin, J.-F. Dong, J. Luo, J.-W. Li, W. Liu, G. Tan, X. Tang, J.-F. Li, J. He, and L.-D. Zhao, Science **373**(6554), 556–561 (2021).
[83]S. Hao, F. Shi, V. P. Dravid, M. G. Kanatzidis, and C. Wolverton, Chem. Mater. **28**(9), 3218–3226 (2016).
[84]G. Xiao, Y. Wang, J. Ning, Y. Wei, B. Liu, W. W. Yu, G. Zou, and B. Zou, RSC Adv. **3**(22), 8104–8130 (2013).
[85]P. D. Antunez, J. J. Buckley, and R. L. Brutchey, Nanoscale **3**(6), 2399–2411 (2011).
[86]D. Bräuhaus, C. Schindler, U. Böttger, and R. Waser, Thin Solid Films **516**(6), 1223–1226 (2008).
[87]X. Zhang, J. Shen, S. Lin, J. Li, Z. Chen, W. Li, and Y. Pei, J. Materiomics **2**(4), 331–337 (2016).
[88]L. Shaabani, S. Aminorroaya-Yamini, J. Byrnes, A. Akbar Nezhad, and G. R. Blake, ACS Omega **2**(12), 9192–9198 (2017).
[89]V. F. Gustiani, L. Septiany, A. A. Nugroho, and G. R. Blake, J. Phys.: Conf. Ser. **1245**(1), 012094 (2019).
[90]H. Yu, D. Gao, X. Wang, X. Du, X. Lin, W. Guo, R. Zou, C. Jin, K. Li, and Y. Chen, NPG Asia Mater. **10**(9), 882–887 (2018).
[91]Z. Huang, S. A. Miller, B. Ge, M. Yan, S. Anand, T. Wu, P. Nan, Y. Zhu, W. Zhuang, G. J. Snyder, P. Jiang, and X. Bao, Angew. Chem., Int. Ed. **56**(45), 14113–14118 (2017).

01 October 2024 06:40:17

Published under an exclusive license by AIP Publishing

[92]M. Yan, X. Tan, Z. Huang, G. Liu, P. Jiang, and X. Bao, J. Mater. Chem. A **6**(18), 8215–8220 (2018).
[93]D. Sarkar, S. Roychowdhury, R. Arora, T. Ghosh, A. Vasdev, B. Joseph, G. Sheet, U. V. Waghmare, and K. Biswas, Angew. Chem., Int. Ed. **60**(18), 10350–10358 (2021).
[94]D. Sarkar, T. Ghosh, S. Roychowdhury, R. Arora, S. Sajan, G. Sheet, U. V. Waghmare, and K. Biswas, J. Am. Chem. Soc. **142**(28), 12237–12244 (2020).
[95]M. Sist, C. Gatti, P. Nørby, S. Cenedese, H. Kasai, K. Kato, and B. B. Iversen, Chem. - Eur. J. **23**(28), 6888–6895 (2017).
[96]V. L. Deringer, R. P. Stoffel, and R. Dronskowski, Phys. Rev. B **89**(9), 094303 (2014).
[97]Y. Zhou, J. Cheng, M. Hong, T. Lyu, M. Wang, X. Luo, C. Zhang, F. Liu, and L. Hu, Nano Energy **127**, 109723 (2024).
[98]L.-D. Zhao, S.-H. Lo, Y. Zhang, H. Sun, G. Tan, C. Uher, C. Wolverton, V. P. Dravid, and M. G. Kanatzidis, Nature **508**(7496), 373–377 (2014).
[99]Z. Wang, H. Wu, B. Zhang, L. Dai, Y. Huo, Y. Huang, G. Han, X. Lu, X. Zhou, and G. Wang, Adv. Funct. Mater. **32**(26), 2111238 (2022).
[100]L. Hu, B. Duan, T. Lyu, N. Lin, C. Zhang, F. Liu, J. Li, M. Wuttig, and Y. Yu, Adv. Funct. Mater. **33**(17), 2214854 (2023).
[101]Z. Wang, H. Wu, M. Xi, H. Zhu, L. Dai, Q. Xiong, G. Wang, G. Han, X. Lu, X. Zhou, and G. Wang, ACS Appl. Mater. Interfaces **12**(37), 41381–41389 (2020).
[102]B. Duan, Y. Zhang, Q. Yang, Y. Li, J. Cheng, C. Zhang, J. Li, F. Liu, and L. Hu, Adv. Energy Sustainability Res. **3**(11), 2200124 (2022).
[103]Y. Huang, T. Lyu, M. Zeng, M. Wang, Y. Yu, C. Zhang, F. Liu, M. Hong, and L. Hu, Interdiscip. Mater. **3**(4), 607–620 (2024).
[104]W. Yao, Y. Zhang, T. Lyu, W. Huang, N. Huang, X. Li, C. Zhang, F. Liu, M. Wuttig, Y. Yu, M. Hong, and L. Hu, Innovation **4**(6), 100522 (2023).
[105]X. Li, Z. Liang, J. Li, F. Cheng, J. He, C. Zhang, J. Li, F. Liu, T. Lyu, B. Ge, and L. Hu, Nano Energy **100**, 107434 (2022).
[106]M. Guo, H.-H. Cui, W. Guo, Z. Chen, H. Ming, Z.-Z. Luo, and Z. Zou, Adv. Funct. Mater. **34**(18), 2313720 (2024).
[107]M. Yan, H. Geng, P. Jiang, and X. Bao, J. Energy Chem. **45**, 83–90 (2020).
[108]T. Lyu, X. Li, Q. Yang, J. Cheng, Y. Zhang, C. Zhang, F. Liu, J. Li, W. Ao, H. Xie, and L. Hu, Chem. Eng. J. **442**, 136332 (2022).
[109]Y.-G. Li, Y.-Q. Liu, M.-R. Wang, W.-Q. Yao, X.-H. Luo, T. Lyu, W.-Q. Ao, C.-H. Zhang, F.-S. Liu, and L.-P. Hu, Rare Met. (published online).
[110]X.-H. Luo, J.-H. Cheng, B.-C. Duan, M.-R. Wang, Y.-W. Zhou, T. Lyu, C.-H. Zhang, S.-N. Zhang, F.-S. Liu, and L.-P. Hu, Rare Met. (published online) (2024).
[111]S. Roychowdhury, T. Ghosh, R. Arora, U. V. Waghmare, and K. Biswas, Angew. Chem., Int. Ed. **57**(46), 15167–15171 (2018).
[112]H. Wiedemeier and P. A. Siemers, Z. Anorg. Allg. Chem. **411**(1), 90–96 (1975).
[113]M. Xu, S. Jakobs, R. Mazzarello, J.-Y. Cho, Z. Yang, H. Hollermann, D. Shang, X. Miao, Z. Yu, L. Wang, and M. Wuttig, J. Phys. Chem. C **121**(45), 25447–25454 (2017).
[114]C.-F. Schön, S. van Bergerem, C. Mattes, A. Yadav, M. Grohe, L. Kobbelt, and M. Wuttig, Sci. Adv. **8**(47), eade0828 (2022).
[115]D. Lencer, M. Salinga, B. Grabowski, T. Hickel, J. Neugebauer, and M. Wuttig, Nat. Mater. **7**(12), 972–977 (2008).
[116]L. Guarneri, S. Jakobs, A. von Hoegen, S. Maier, M. Xu, M. Zhu, S. Wahl, C. Teichrib, Y. Zhou, O. Cojocaru-Mirédin, M. Raghuwanshi, C.-F. Schön, M. Drögeler, C. Stampfer, R. P. S. M. Lobo, A. Piarristeguy, A. Pradel, J.-Y. Raty, and M. Wuttig, Adv. Mater. **33**(39), 2102356 (2021).
[117]S. Maier, S. Steinberg, Y. Cheng, C.-F. Schön, M. Schumacher, R. Mazzarello, P. Golub, R. Nelson, O. Cojocaru-Mirédin, J.-Y. Raty, and M. Wuttig, Adv. Mater. **32**(49), 2005533 (2020).
[118]J.-Y. Raty, M. Schumacher, P. Golub, V. L. Deringer, C. Gatti, and M. Wuttig, Adv. Mater. **31**(3), 1806280 (2019).
[119]G. N. Lewis, J. Am. Chem. Soc. **38**(4), 762–785 (1916).
[120]M. Cagnoni, D. Führen, and M. Wuttig, Adv. Mater. **30**(33), 1801787 (2018).
[121]M. Wuttig, C.-F. Schön, J. Lötfering, P. Golub, C. Gatti, and J.-Y. Raty, Adv. Mater. **35**(20), 2208485 (2023).
[122]Y. Yu, C. Zhou, T. Ghosh, C.-F. Schön, Y. Zhou, S. Wahl, M. Raghuwanshi, P. Kerres, C. Bellin, A. Shukla, O. Cojocaru-Mirédin, and M. Wuttig, Adv. Mater. **35**(19), 2300893 (2023).
[123]J.-Y. Raty and M. Wuttig, J. Phys. D: Appl. Phys. **53**(23), 234002 (2020).
[124]R. Arora, U. V. Waghmare, and C. N. R. Rao, Adv. Mater. **35**(7), 2208724 (2023).
[125]Y. Yu, O. Cojocaru-Mirédin, and M. Wuttig, Phys. Status Solidi A (published online).
[126]D. An, S. Zhang, X. Zhai, W. Yang, R. Wu, H. Zhang, W. Fan, W. Wang, S. Chen, O. Cojocaru-Mirédin, X.-M. Zhang, M. Wuttig, and Y. Yu, Nat. Commun. **15**(1), 3177 (2024).
[127]Y. Cheng, O. Cojocaru-Mirédin, J. Keutgen, Y. Yu, M. Küpers, M. Schumacher, P. Golub, J.-Y. Raty, R. Dronskowski, and M. Wuttig, Adv. Mater. **31**(43), 1904316 (2019).
[128]M. Raghuwanshi, O. Cojocaru-Mirédin, and M. Wuttig, Nano Lett. **20**(1), 116–121 (2020).
[129]M. Zhu, O. Cojocaru-Mirédin, A. M. Mio, J. Keutgen, M. Küpers, Y. Yu, J.-Y. Cho, R. Dronskowski, and M. Wuttig, Adv. Mater. **30**(18), 1706735 (2018).
[130]C. Rodenkirchen, M. Cagnoni, S. Jakobs, Y. Cheng, J. Keutgen, Y. Yu, M. Wuttig, and O. Cojocaru-Mirédin, Adv. Funct. Mater. **30**(17), 1910039 (2020).
[131]M. Wuttig, V. L. Deringer, X. Gonze, C. Bichara, and J.-Y. Raty, Adv. Mater. **30**(51), 1803777 (2018).
[132]A. M. Elkorashy, Phys. Status Solidi B **135**(2), 707–713 (1986).
[133]D. Vaughn, I. I. D. Sun, S. M. Levin, A. J. Biacchi, T. S. Mayer, and R. E. Schaak, Chem. Mater. **24**(18), 3643–3649 (2012).
[134]E. O. Kane, J. Phys. Chem. Solids **1**(4), 249–261 (1957).
[135]Y. Pei, A. D. LaLonde, H. Wang, and G. J. Snyder, Energy Environ. Sci. **5**(7), 7963–7969 (2012).
[136]Y. Pei, A. F. May, and G. J. Snyder, Adv. Energy Mater. **1**(2), 291–296 (2011).
[137]Y. Pei, X. Shi, A. LaLonde, H. Wang, L. Chen, and G. J. Snyder, Nature **473**(7345), 66–69 (2011).
[138]J. Li, Z. Chen, X. Zhang, Y. Sun, J. Yang, and Y. Pei, NPG Asia Mater. **9**(3), e353–e353 (2017).
[139]K. Yuan, Z. Sun, X. Zhang, X. Gong, and D. Tang, Phys. Chem. Chem. Phys. **22**(4), 1911–1922 (2020).
[140]J. M. Skelton, J. Mater. Chem. C **9**(35), 11772–11787 (2021).
[141]U. Argaman, R. E. Abutbul, E. Segev, and G. Makov, CrystEngComm **19**(41), 6107–6115 (2017).
[142]Q. Fan, J. Yang, J. Cao, and C. Liu, R. Soc. Open Sci. **8**(6), 201980 (2021).
[143]D. Sarkar, M. Samanta, T. Ghosh, K. Dolui, S. Das, K. Saurabh, D. Sanyal, and K. Biswas, Energy Environ. Sci. **15**(11), 4625–4635 (2022).
[144]M. Li, Q. Sun, S.-D. Xu, M. Hong, W.-Y. Lyu, J.-X. Liu, Y. Wang, M. Dargusch, J. Zou, and Z.-G. Chen, Adv. Mater. **33**(40), 2102575 (2021).
[145]T. Xing, C. Zhu, Q. Song, H. Huang, J. Xiao, D. Ren, M. Shi, P. Qiu, X. Shi, F. Xu, and L. Chen, Adv. Mater. **33**(17), 2008773 (2021).
[146]M. Hong, W. Lyv, M. Li, S. Xu, Q. Sun, J. Zou, and Z.-G. Chen, Joule **4**(9), 2030–2043 (2020).
[147]T. Jin, L. Yang, X. Zhang, W. Li, and Y. Pei, InfoMat **6**(2), e12502 (2024).
[148]T. Oku, H. Funashima, S. Kawaguchi, Y. Kubota, and A. Kosuga, Mater. Today Phys. **20**, 100484 (2021).
[149]B. Qin, D. Wang, W. He, Y. Zhang, H. Wu, S. J. Pennycook, and L.-D. Zhao, J. Am. Chem. Soc. **141**(2), 1141–1149 (2019).
[150]Z. Chen, Q. Sun, F. Zhang, J. Mao, Y. Chen, M. Li, Z.-G. Chen, and R. Ang, Mater. Today Phys. **17**, 100340 (2021).
[151]W.-D. Liu, D.-Z. Wang, Q. Liu, W. Zhou, Z. Shao, and Z.-G. Chen, Adv. Energy Mater. **10**(19), 2000367 (2020).
[152]H. Pang, Y. Qiu, D. Wang, Y. Qin, R. Huang, Z. Yang, X. Zhang, and L.-D. Zhao, J. Am. Chem. Soc. **143**(23), 8538–8542 (2021).
[153]J. Li, Z. Chen, X. Zhang, H. Yu, Z. Wu, H. Xie, Y. Chen, and Y. Pei, Adv. Sci. **4**(12), 1700341 (2017).
[154]X. Zhang, J. Li, X. Wang, Z. Chen, J. Mao, Y. Chen, and Y. Pei, J. Am. Chem. Soc. **140**(46), 15883–15888 (2018).
[155]A. F. May, E. S. Toberer, A. Saramat, and G. J. Snyder, Phys. Rev. B **80**(12), 125205 (2009).
[156]W.-W. Hu, J.-C. Sun, Y. Zhang, Y. Gong, Y.-T. Fan, X.-F. Tang, and G.-J. Tan, Acta Phys. Sin. **71**(4), 047101 (2022).
[157]J. Dong, Y. Liu, Z. Li, H. Xie, Y. Jiang, H. Wang, X. Y. Tan, A. Suwardi, X. Zhou, J.-F. Li, C. Wolverton, V. P. Dravid, Q. Yan, and M. G. Kanatzidis, J. Am. Chem. Soc. **146**(25), 17355–17364 (2024).
[158]B.-S. Du, J.-K. Jian, H.-T. Liu, J. Liu, and L. Qiu, Chin. Phys. B **27**(4), 048102 (2018).
[159]H. Wang, E. Schechtel, Y. Pei, and G. J. Snyder, Adv. Energy Mater. **3**(4), 488–495 (2013).

01 October 2024 06:40:17

Published under an exclusive license by AIP Publishing

[160]W. Li, L. Zheng, B. Ge, S. Lin, X. Zhang, Z. Chen, Y. Chang, and Y. Pei, Adv. Mater. **29**(17), 1605887 (2017).
[161]L.-D. Zhao, C. Chang, G. Tan, and M. G. Kanatzidis, Energy Environ. Sci. **9**(10), 3044–3060 (2016).
[162]M. Hong, Z.-G. Chen, L. Yang, Y.-C. Zou, M. S. Dargusch, H. Wang, and J. Zou, Adv. Mater. **30**(11), 1705942 (2018).
[163]Y.-M. Han, J. Zhao, M. Zhou, X.-X. Jiang, H.-Q. Leng, and L.-F. Li, J. Mater. Chem. A **3**(8), 4555–4559 (2015).
[164]M. Hong, M. Li, Y. Wang, X.-L. Shi, and Z.-G. Chen, Adv. Mater. **35**(2), 2208272 (2023).
[165]L. D. Zhao, H. J. Wu, S. Q. Hao, C. I. Wu, X. Y. Zhou, K. Biswas, J. Q. He, T. P. Hogan, C. Uher, C. Wolverton, V. P. Dravid, and M. G. Kanatzidis, Energy Environ. Sci. **6**(11), 3346–3355 (2013).
[166]J. Cai, R. Wang, S. Zhuang, F. Gao, M. Zhang, Z. Zhang, X. Tan, G. Liu, and J. Jiang, Adv. Funct. Mater. **34**(17), 2311217 (2024).
[167]K. Li, L. Sun, W. Bai, N. Ma, C. Zhao, J. Zhao, C. Xiao, and Y. Xie, J. Am. Chem. Soc. **146**(20), 14318–14327 (2024).
[168]Z. Guo, G. Wu, X. Tan, R. Wang, Z. Zhang, G. Wu, Q. Zhang, J. Wu, G.-Q. Liu, and J. Jiang, Adv. Funct. Mater. **33**(11), 2212421 (2023).
[169]D.-Z. Wang, W.-D. Liu, M. Li, K. Zheng, H. Hu, L.-C. Yin, Y. Wang, H. Zhu, X.-L. Shi, X. Yang, Q. Liu, and Z.-G. Chen, Adv. Funct. Mater. **33**(14), 2213040 (2023).
[170]Y. Zheng, T. J. Slade, L. Hu, X. Y. Tan, Y. Luo, Z.-Z. Luo, J. Xu, Q. Yan, and M. G. Kanatzidis, Chem. Soc. Rev. **50**(16), 9022–9054 (2021).
[171]S. I. Kim, K. H. Lee, H. A. Mun, H. S. Kim, S. W. Hwang, J. W. Roh, D. J. Yang, W. H. Shin, X. S. Li, Y. H. Lee, G. J. Snyder, and S. W. Kim, Science **348**(6230), 109–114 (2015).
[172]Z. Chen, X. Zhang, and Y. Pei, Adv. Mater. **30**(17), 1705617 (2018).
[173]Y. Yu, M. Cagnoni, O. Cojocaru-Mirédin, and M. Wuttig, Adv. Funct. Mater. **30**(8), 1904862 (2020).
[174]Y. Zhang, X. Ke, C. Chen, J. Yang, and P. R. C. Kent, Phys. Rev. B **80**(2), 024304 (2009).
[175]O. Delaire, J. Ma, K. Marty, A. F. May, M. A. McGuire, M. H. Du, D. J. Singh, A. Podlesnyak, G. Ehlers, M. D. Lumsden, and B. C. Sales, Nat. Mater. **10**(8), 614–619 (2011).
[176]F. Zhang, R. Li, L. Gan, X. Tan, S. He, B. Tian, and R. Ang, Sci. China Mater. **66**(9), 3659–3669 (2023).
[177]Y. Tian, L. Ma, Z. Zhou, G.-K. Ren, Y. Li, Z. Wei, Y. Shi, Y. Zhao, and Y.-H. Lin, J. Mater. Chem. A **12**(25), 15177–15185 (2024).
[178]J. He, S. N. Girard, M. G. Kanatzidis, and V. P. Dravid, Adv. Funct. Mater. **20**(5), 764–772 (2010).
[179]S. Lee, K. Esfarjani, T. Luo, J. Zhou, Z. Tian, and G. Chen, Nat. Commun. **5**(1), 3525 (2014).
[180]S. Perumal, M. Samanta, T. Ghosh, U. S. Shenoy, A. K. Bohra, S. Bhattacharya, A. Singh, U. V. Waghmare, and K. Biswas, Joule **3**(10), 2565–2580 (2019).
[181]Y. Fan, C. Xie, J. Li, X. Meng, J. Sun, J. Wu, X. Tang, and G. Tan, Energy Environ. Mater. **7**(2), e12535 (2024).
[182]B. Jabar, F. Li, Z. Zheng, A. Mansoor, Y. Zhu, C. Liang, D. Ao, Y. Chen, G. Liang, P. Fan, and W. Liu, Nat. Commun. **12**(1), 7192 (2021).

01 October 2024 06:40:17

Published under an exclusive license by AIP Publishing